A&A 520, A83 (2010)
DOI: 10.1051/0004-6361/201014484

Astronomy & Astrophysics

VHE γ-ray emission of PKS 2155–304: spectral and temporal variability

HESS Collaboration, A. Abramowski[4], F. Acero[15], F. Aharonian[1,13], A. G. Akhperjanian[2], G. Anton[16], U. Barres de Almeida[8,⋆], A. R. Bazer-Bachi[3], Y. Becherini[12], B. Behera[14], W. Benbow[1], K. Bernlöhr[1,5], A. Bochow[1], C. Boisson[6], J. Bolmont[19], V. Borrel[3], J. Brucker[16], F. Brun[19], P. Brun[7], R. Bühler[1], T. Bulik[29], I. Büsching[9], T. Boutelier[17], P. M. Chadwick[8], A. Charbonnier[19], R. C. G. Chaves[1], A. Cheesebrough[8], L.-M. Chounet[10], A. C. Clapson[1], G. Coignet[11], J. Conrad[31], L. Costamante[1,34], M. Dalton[5], M. K. Daniel[8], I. D. Davids[22,9], B. Degrange[10], C. Deil[1], H. J. Dickinson[8], A. Djannati-Ataï[12], W. Domainko[1], L. O'C. Drury[13], F. Dubois[11], G. Dubus[17], J. Dyks[24], M. Dyrda[28], K. Egberts[1,30], P. Eger[16], P. Espigat[12], L. Fallon[13], C. Farnier[15], S. Fegan[10], F. Feinstein[15], M. V. Fernandes[4], A. Fiasson[11], A. Förster[1], G. Fontaine[10], M. Füßling[5], S. Gabici[13], Y. A. Gallant[15], L. Gérard[12], D. Gerbig[21], B. Giebels[10], J. F. Glicenstein[7], B. Glück[16], P. Goret[7], D. Göring[16], D. Hampf[4], M. Hauser[14], S. Heinz[16], G. Heinzelmann[4], G. Henri[17], G. Hermann[1], J. A. Hinton[33], A. Hoffmann[18], W. Hofmann[1], P. Hofverberg[1], M. Holleran[9], S. Hoppe[1], D. Horns[4], A. Jacholkowska[19], O. C. de Jager[9], C. Jahn[16], I. Jung[16], K. Katarzyński[27], U. Katz[16], S. Kaufmann[14], M. Kerschhaggl[5], D. Khangulyan[1], B. Khélifi[10], D. Keogh[8], D. Klochkov[18], W. Kluźniak[24], T. Kneiske[4], Nu. Komin[7], K. Kosack[7], R. Kossakowski[11], G. Lamanna[11], J.-P. Lenain[6], T. Lohse[5], C.-C. Lu[1], V. Marandon[12], A. Marcowith[15], J. Masbou[11], D. Maurin[19], T. J. L. McComb[8], M. C. Medina[6], J. Méhault[15], R. Moderski[24], E. Moulin[7], M. Naumann-Godo[10], M. de Naurois[19], D. Nedbal[20], D. Nekrassov[1], N. Nguyen[4], B. Nicholas[26], J. Niemiec[28], S. J. Nolan[8], S. Ohm[1], J.-F. Olive[3], E. de Oña Wilhelmi[1], B. Opitz[4], K. J. Orford[8], M. Ostrowski[23], M. Panter[1], M. Paz Arribas[5], G. Pedaletti[14], G. Pelletier[17], P.-O. Petrucci[17], S. Pita[12], G. Pühlhofer[18], M. Punch[12], A. Quirrenbach[14], B. C. Raubenheimer[9], M. Raue[1,34], S. M. Rayner[8], O. Reimer[30], M. Renaud[12], R. de los Reyes[1], F. Rieger[1,34], J. Ripken[31], L. Rob[20], S. Rosier-Lees[11], G. Rowell[26], B. Rudak[24], C. B. Rulten[8], J. Ruppel[21], F. Ryde[32], V. Sahakian[2], A. Santangelo[18], R. Schlickeiser[21], F. M. Schöck[16], A. Schönwald[5], U. Schwanke[5], S. Schwarzburg[18], S. Schwemmer[14], A. Shalchi[21], I. Sushch[5], M. Sikora[24], J. L. Skilton[25], H. Sol[6], Ł. Stawarz[23], R. Steenkamp[22], C. Stegmann[16], F. Stinzing[16], G. Superina[10], A. Szostek[23,17], P. H. Tam[14], J.-P. Tavernet[19], R. Terrier[12], O. Tibolla[1], M. Tluczykont[4], K. Valerius[16], C. van Eldik[1], G. Vasileiadis[15], C. Venter[9], L. Venter[6], J. P. Vialle[11], A. Viana[7], P. Vincent[19], M. Vivier[7], H. J. Völk[1], F. Volpe[1,10], S. Vorobiov[15], S. J. Wagner[14], M. Ward[8], A. A. Zdziarski[24], A. Zech[6], and H.-S. Zechlin[4]
(Affiliations can be found after the references)

Received 22 March 2010 / Accepted 14 May 2010

ABSTRACT

Context. Observations of very high-energy γ-rays from blazars provide information about acceleration mechanisms occurring in their innermost regions. Studies of variability in these objects lead to a better understanding of the mechanisms in play.
Aims. To investigate the spectral and temporal variability of VHE (>100 GeV) γ-rays of the well-known high-frequency-peaked BL Lac object PKS 2155−304 with the HESS imaging atmospheric Cherenkov telescopes over a wide range of flux states.
Methods. Data collected from 2005 to 2007 were analyzed. Spectra were derived on time scales ranging from 3 years to 4 min. Light curve variability was studied through doubling timescales and structure functions and compared with red noise process simulations.
Results. The source was found to be in a low state from 2005 to 2007, except for a set of exceptional flares that occurred in July 2006. The quiescent state of the source is characterized by an associated mean flux level of $(4.32 \pm 0.09_{\rm stat} \pm 0.86_{\rm syst}) \times 10^{-11}$ cm^{-2} s^{-1} above 200 GeV, or approximately 15% of the Crab Nebula, and a power-law photon index of $\Gamma = 3.53 \pm 0.06_{\rm stat} \pm 0.10_{\rm syst}$. During the flares of July 2006, doubling timescales of ∼2 min are found. The spectral index variation is examined over two orders of magnitude in flux, yielding different behavior at low and high fluxes, which is a new phenomenon in VHE γ-ray emitting blazars. The variability amplitude characterized by the fractional rms $F_{\rm var}$ is strongly energy-dependent and is $\propto E^{0.19\pm0.01}$. The light curve rms correlates with the flux. This is the signature of a multiplicative process that can be accounted for as a red noise with a Fourier index of ∼2.
Conclusions. This unique data set shows evidence of a low-level γ-ray emission state from PKS 2155−304 that possibly has a different origin than the outbursts. The discovery of the light curve lognormal behavior might be an indicator of the origin of aperiodic variability in blazars.

Key words. gamma rays: general – galaxies: active – galaxies: jets – BL Lacertae objects: individual: PKS 2155−304

1. Introduction

The BL Lacertae (BL Lac) category of active galactic nuclei (AGN) represents the vast majority of the population of energetic

⋆ Supported by CAPES Foundation, Ministry of Education of Brazil.

and extremely variable extragalactic very high-energy γ-ray emitters. Their luminosity varies in unpredictable, highly irregular ways, by orders of magnitude and at all wavelengths across the electromagnetic spectrum. The very high-energy (VHE, $E \geq 100$ GeV) γ-ray fluxes vary often on the shortest timescales that can be seen in this type of object, with large amplitudes that can dominate the overall output. It thus indicates that the understanding of this energy domain is the most important one for understanding the underlying fundamental variability and emission mechanisms in play in high flux states.

It has been difficult, however, to ascertain whether γ-ray emission is present only during high flux states or also when the source is in a more stable or quiescent state but with a flux that is below the instrumental limits. The advent of the current generation of atmospheric Cherenkov telescopes with unprecedented sensitivity in the VHE regime gives new insight into these questions.

The high-frequency-peaked BL Lac object (HBL) PKS 2155−304, located at redshift $z = 0.117$, initially discovered as a VHE γ-ray emitter by the Mark 6 telescope (Chadwick et al. 1999), has been detected by the first HESS telescope in 2002−2003 (Aharonian et al. 2005b). It has been frequently observed by the full array of four telescopes since 2004, either sparsely during the HESS monitoring program or intensely during dedicated campaigns, such as described in Aharonian et al. (2005c), showing mean flux levels of ∼20% of the Crab Nebula flux for energies above 200 GeV. During the summer of 2006, PKS 2155−304 exhibited unprecedented flux levels accompanied by strong variability (Aharonian et al. 2007a), making temporal and spectral variability studies possible on timescales on the order of a few minutes. The VHE γ-ray emission is usually thought to originate from a relativistic jet, emanating from the vicinity of a supermassive black hole (SMBH). The physical processes in play are still poorly understood, but the analysis of the γ-ray flux spectral and temporal characteristics is well-suited to providing deeper insight.

For this goal, the data set of HESS observations of PKS 2155−304 between 2005 and 2007 is used. After describing the observations and the analysis chain in Sect. 2, the emission from the "quiescent", i.e. nonflaring, state of the source is characterized in Sect. 3. Section 4 explains the spectral variability related to the source intensity. Section 5 describes the temporal variability during the highly active state of the source and its possible energy dependence. Section 6 illustrates the observed variability phenomenon by a random stationary process, characterized by a simple power density spectrum. Section 7 shows how limits on the characteristic time of the source can be derived. The multi-wavelength aspects from the high flux state will be presented in a second paper.

2. Observations and analysis

HESS is an array of four imaging atmospheric Cherenkov telescopes situated in the Khomas Highland of Namibia (23°16′18″ South, 16°30′00″ East), at an elevation of 1800 m above sea level (see Aharonian et al. 2006). PKS 2155−304 was observed by HESS each year after 2002; results of observations in 2002, 2003, and 2004 can be found in Aharonian et al. (2005b), Aharonian et al. (2005c) and Giebels et al. (2005). The data reported here were collected between 2005 and 2007. In 2005, 12.2 h of observations were taken. A similar observation time was scheduled in 2006, but following the strong flare of July 26 (Aharonian et al. 2007a), it was decided to increase this observation time significantly. Ultimately, from June to October 2006, this source was observed for 75.9 h, with a further 20.9 h in 2007.

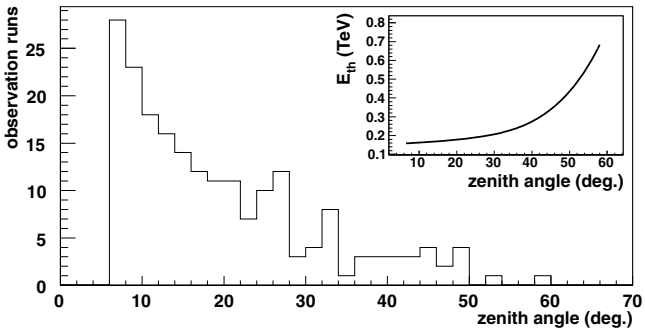

Fig. 1. Zenith angle distribution for the 202 4-telescopes observation runs from 2005 to 2007. The inset shows, for each zenith angle, the energy threshold associated with the analysis presented in Sect. 2.

Table 1. Summary of observations for each year.

Year	T	n_{on}	n_{off}	Excess	σ	$\sigma/\sqrt{T}$
2005	9.4	7282	27 071	1868	21.8	7.1
2006	66.1	123 567	203 815	82 804	288.4	35.5
2007	13.8	11 012	40 065	2999	28.6	7.7
Total	89.2	141 861	270 951	87 671	275.6	29.2

Notes. T represents the live-time (hours), n_{on} the number of on-source events, n_{off} the number of off-source events (from a region five times larger than for the on-source events), and σ the significance of the corresponding excess, given in units of standard deviations.

The data were recorded during runs of 28 min nominal duration, with the telescopes pointing at 0.5° from the source position in the sky to enable a simultaneous estimate of the background. This offset was taken alternatively in both right ascension and declination (with both signs), in order to minimize systematics. Only the runs passing the HESS data-quality selection criteria were used for the analyses presented below. These criteria imply good atmospheric conditions and checks that the hardware state of the cameras is satisfactory. The number of runs thus selected is 22 for 2005, 153 for 2006, and 35 for 2007, corresponding to live-times of 9.4, 66.1, and 13.8 h respectively. During these observations, zenith angles were between 7 and 60 degrees, resulting in large variations in the instrument energy threshold (E_{th}, see Fig. 1) and sensitivity. This variation has been accounted for in the spectral and temporal variability studies presented below.

The data have been analyzed following the prescription presented in Aharonian et al. (2006), using the *loose* set of cuts that are well adapted for bright sources with moderately soft spectra, and the *Reflected-Region* method for the definition of the on-source and off-source data regions. A year-wise summary of the observations and the resulting detections are shown in Table 1. A similar summary is given in Appendix A for the 67 nights of data taken, showing that the emission of PKS 2155−304 is easily detected by HESS almost every night. For 66 nights out of 67, the significance per square root of the live-time ($\sigma/\sqrt{T}$, where T is the observation live-time) is at least equal to $3.6\sigma/\sqrt{h}$, the only night with a lower value – MJD 53705 – corresponding to a very short exposure. In addition, for 61 nights out of 67 the source emission is high enough to enable a detection of the source with 5σ significance in one hour or less, a level usually required in this domain to firmly claim a new source detection. In 2006 the source exhibits very strong activity (38 nights,

Table 2. The various data sets used in the paper, referred to in the text by the labels presented in this table.

Label	Period	Runs	T(hours)	Excess	σ	Section	Additional criteria
D	2005–2007	165	69.7	67 654	237.4	4, 7	–
$D_{\rm QS}$	2005–2007	115	48.1	12 287	60.5	3.2, 3.4, 3.3, 7	July 2006 excluded
$D_{\rm QS-2005}$	2005	19	8.0	1816	22.6	3.4	–
$D_{\rm QS-2006}$	2006	61	26.3	7472	48.4	3.4	July 2006 excluded
$D_{\rm QS-2007}$	2007	35	13.8	2999	28.6	3.4	–
$D_{\rm JULY06}$	July 2006	50	21.6	55,367	281.8	4, 5, 6, 7	–
$D_{\rm FLARES}$	July 2006 (4 nights)	27	11.8	46 036	284.1	4, 5, 6, 7	–

Notes. Only runs with the full array of four telescopes in operation (202 runs over 210) and an energy threshold lower than 200 GeV (165 runs over 202) are considered. The corresponding period of the observations, the number of runs, the live-time T (hours), the number of γ excess events and its significance σ are shown. The column *section* indicates the sections of the paper in which each data set is discussed. Additional criteria for the data set definitions are indicated in the last column.

between MJD 53916–53999) with a nightly $\sigma/\sqrt{T}$ varying from 3.6 to 150, and being higher than $10\sigma/\sqrt{h}$ for 19 nights. The activity of the source climaxes on MJD 53944 and 53946 with statistical significances that are unprecedented at these energies, the rate of detected γ-rays corresponding to 2.5 and 1.3 Hz, with 150 and $98\sigma/\sqrt{h}$ respectively.

For subsequent spectral analysis, an improved energy reconstruction method with respect to the one described in Aharonian et al. (2006) was applied. This method is based on a look-up table determined from Monte-Carlo simulations, which contains the relation between an image's amplitude and its reconstructed impact parameter as a function of the true energy, the observation zenith angle, the position of the source in the camera, the optical efficiency of the telescopes (which tend to decrease due to the aging of the optical surfaces), the number of triggered telescopes and the reconstructed altitude of the shower maximum. Thus, for a given event, the reconstructed energy is determined by requiring the minimal χ^2 between the image amplitudes and those expected from the look-up table corresponding to the same observation conditions. This method yields a slightly lower energy threshold (shown in Fig. 1 as a function of zenith angle), an energy resolution that varies from 15% to 20% over all the energy range, and biases in the energy reconstruction that are smaller than 5%, even close to the threshold. The systematic uncertainty in the normalization of the HESS energy scale is estimated to be as large as 15%, corresponding for such soft spectrum source to 40% in the overall flux normalization as quoted in Aharonian et al. (2009).

All the spectra presented in this paper have been obtained using a forward-folding maximum likelihood method based on the measured energy-dependent on-source and off-source distributions. This method, fully described in Piron et al. (2001), performs a global deconvolution of the instrument functions (energy resolution, collection area) and the parametrization of the spectral shape. Two different sets of parameters, corresponding to a power law and to a power law with an exponential cut-off, are used for the spectral shape, with the following equations:

$$\phi(E) = \phi_0 \left(\frac{E}{E_0}\right)^{-\Gamma} \tag{1}$$

$$\phi(E) = \phi_0 \exp\left(\frac{E_0}{E_{\rm cut}}\right)\left(\frac{E}{E_0}\right)^{-\Gamma} \exp\left(-\frac{E}{E_{\rm cut}}\right) \tag{2}$$

ϕ_0 represents the differential flux at E_0 (chosen to be 1 TeV), Γ is the power-law index and $E_{\rm cut}$ the characteristic energy of the exponential cut-off. The maximum likelihood method provides the best set of parameters corresponding to the selected hypothesis, and the corresponding error matrix.

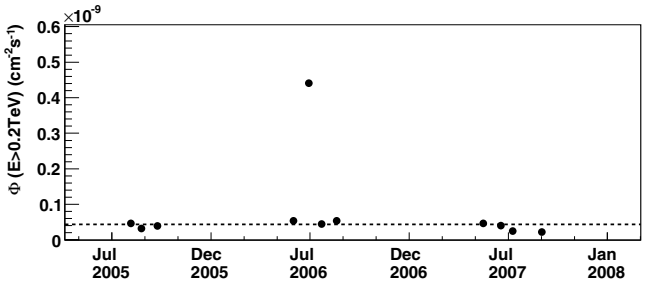

Fig. 2. Monthly averaged integral flux of PKS 2155−304 above 200 GeV obtained from data set D (see Table 2). The dotted line corresponds to 15% of the Crab Nebula emission level (see Sect. 3.2).

Finally, various data sets have been used for subsequent analyses. These are summarized in Table 2.

3. Characterization of the quiescent state

As can be seen in Fig. 2, with the exception of the high state of July 2006 PKS 2155−304 was in a low state during the observations from 2005 to 2007. This section explores the variability of the source during these periods of low-level activity, based on the determination of the run-wise integral fluxes for the data set $D_{\rm QS}$, which excludes the flaring period of July 2006 and also those runs whose energy threshold is higher than 200 GeV (see 3.1 for justification). As for Sects. 5 and 6, the control of systematics in such a study is particularly important, especially because of the strong variations of the energy threshold throughout the observations.

3.1. Method and systematics

The integral flux for a given period of observations is determined in a standard way. For subsequent discussion purposes, the formula applied is given here:

$$\Phi = N_{\rm exp} \frac{\int_{E_{\rm min}}^{E_{\rm max}} S(E){\rm d}E}{T \int_0^\infty \int_{E_{\rm min}}^{E_{\rm max}} A(E)R(E,E')S(E){\rm d}E'{\rm d}E} \tag{3}$$

where T represents the corresponding live-time, $A(E)$ and $R(E, E')$ are, respectively, the collection area at the true energy E and the energy resolution function between E and the measured energy E', and $S(E)$ the shape of the differential energy spectrum as defined in Eqs. (1) and (2). Finally, $N_{\rm exp}$ is the number of measured events in the energy range $[E_{\rm min}, E_{\rm max}]$.

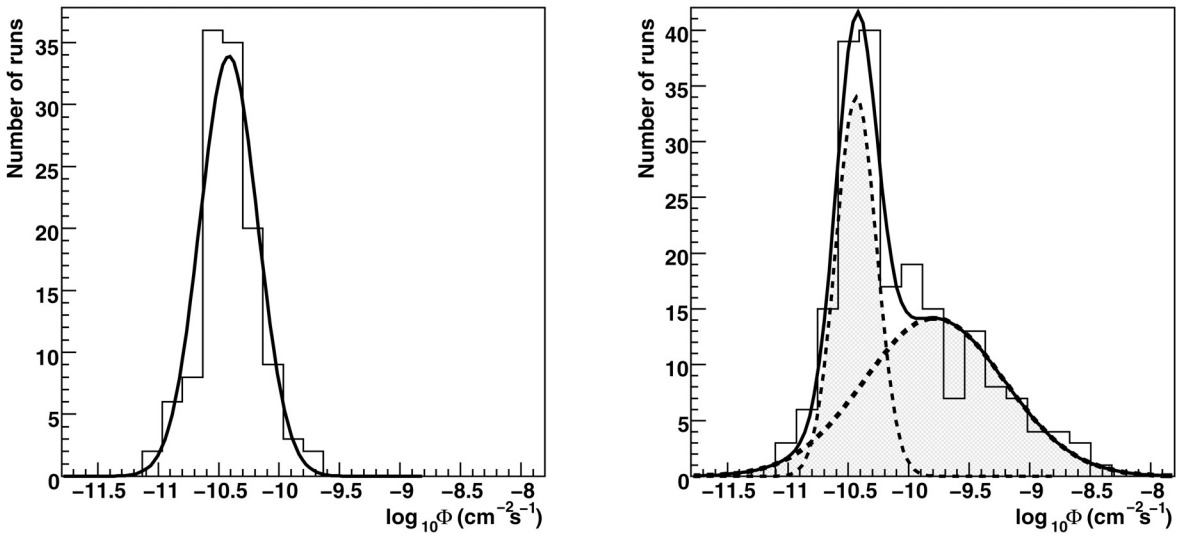

Fig. 3. Distributions of the logarithms of integral fluxes above 200 GeV in individual runs. *Left*: from 2005 to 2007 except the July 2006 period (data set D_{QS}), fitted by a Gaussian. *Right*: all runs from 2005 to 2007 (data set D), where the solid line represents the result of a fit by the sum of 2 Gaussians (dashed lines). See Table 4 for details.

In the case that $S(E)$ is a power law, an important source of systematic error in the determination of the integral flux variation with time comes from the value chosen for the index Γ. The average 2005−2007 energy spectrum yields a very well determined power-law index[1]. However, in Sect. 4 it will be shown that this index varies depending on the flux level of the source. Moreover, in some cases the energy spectrum of the source shows some curvature in the TeV region, giving slight variations in the fitted power-law index depending on the energy range used.

For runs whose energy threshold is lower than E_{min}, a simulation performed under the observation conditions corresponding to the data shows that an index variation of $\Delta\Gamma = 0.1$ implies a flux error at the level of $\Delta\Phi \sim 1\%$, this relation being quite linear up to $\Delta\Gamma \sim 0.5$. However, this relation no longer holds when the energy threshold is above E_{min}, as the determination of Φ becomes much more dependent on the choice of Γ. For this reason, only runs whose energy threshold is lower than E_{min} will be kept for the subsequent light curves. The value of E_{min} is chosen as 200 GeV, which is a compromise between a low value which maximizes the excess numbers used for the flux determinations and a high value which maximizes the number of runs whose energy threshold is lower than E_{min}.

3.2. Run-wise distribution of the integral flux

From 2005 to 2007, PKS 2155−304 is almost always detected when observed (except for two nights for which the exposure was very low), indicating the existence, at least during these observations, of a minimal level of activity of the source. Focussing on data set D_{QS} (which excludes the July 2006 data where the source is in a high state), the distribution of the integral fluxes of the individual runs above 200 GeV has been determined for the 115 runs, using a spectral index $\Gamma = 3.53$ (the best value for this data set, as shown in 3.4). This distribution has an asymmetric shape, with mean value $(4.32 \pm 0.09_{stat}) \times 10^{-11}$ cm^{-2} s^{-1} and root mean square (rms) $(2.48 \pm 0.11_{stat}) \times 10^{-11}$ cm^{-2} s^{-1}, and is very well described with a lognormal function. Such a behavior implies that the logarithm of fluxes follows a normal distribution, centered on the logarithm of $(3.75 \pm 0.11_{stat}) \times 10^{-11}$ cm^{-2} s^{-1}. This is shown in the left panel of Fig. 3, where the solid line represents the best fit obtained with a maximum-likelihood method, yielding results independent of the choice of the intervals in the histogram. It is interesting to note that this result can be compared to the fluxes measured by HESS from PKS 2155−304 during its construction phase, in 2002 and 2003 (see Aharonian et al. 2005b,c). As shown in Table 3, these flux levels extrapolated down to 200 GeV were close to the value corresponding to the peak shown in the left panel of Fig. 3.

Table 3. Integral fluxes and their statistical errors from 2002 and 2003 observations of PKS 2155−304 during the HESS construction phase.

Month	Year	Φ [10^{-11} cm^{-2} s^{-1}]
July	2002	16.4 ± 4.7
Oct.	2002	8.9 ± 5.2
June	2003	5.8 ± 1.4
July	2003	2.9 ± 0.5
Aug.	2003	3.5 ± 0.5
Sep.	2003	4.9 ± 1.2
Oct.	2003	5.2 ± 0.5

Notes. These values are taken from Aharonian et al. (2005b,c) and, correspond to flux extrapolations to above 200 GeV.

The right panel of Fig. 3 shows how the flux distribution is modified when the July 2006 data are taken into account (data set D in Table 2): the histogram can be accounted for by the superposition of two Gaussian distributions (solid curve). The results, summarized in Table 4, are also independent of the choice of the intervals in the histogram. Remarkably enough, the characteristics of the first Gaussian obtained in the first step (left panel) remain quite stable in the double Gaussian fit.

This leads to two conclusions. First, the flux distribution of PKS 2155−304 is well described considering a low state and a high state, for each of which the distribution of the logarithms

[1] The resulting spectral index is $\Gamma = 3.37 \pm 0.02_{stat}$. The alternative hypothesis with a curvature in the spectrum (Eq. (2)) is favored at 8.4σ, yelding a harder index ($\Gamma = 3.05 \pm 0.05_{stat}$) with an exponential cut-off at $E_{cut} = 1.76 \pm 0.27_{stat}$ TeV. As the integral flux is dominated by the low-energy part of the spectrum, the choice of the model has a little effect on the integral flux values above 200 GeV.

Table 4. The distribution of the flux logarithm.

	"Quiescent" regime	Flaring regime
$\langle \log_{10} \Phi \rangle$	–10.42 ± 0.02	–9.79 ± 0.11
rms of $\log_{10} \Phi$	0.24 ± 0.02	0.58 ± 0.04

Notes. First column: distribution as fitted by a single Gaussian law for the "quiescent" regime (data set D_{QS}). Second column: distribution fitted by two Gaussian laws, one for the "quiescent" regime, the other for the flaring regime (data set D). Decimal logarithms are quoted to make the comparison with the left panel of Fig. 3 easier and the flux is expressed in cm^{-2} s^{-1}. In the first line the average of fluxes is reported, while in the second line their rms.

of the fluxes follows a Gaussian distribution. The characteristics of the lognormal flux distribution for the high state are given in Sects. 5–7. Secondly, PKS 2155−304 has a level of minimal activity that seems to be stable on a several-year time-scale. This state will henceforth be referred to as the "quiescent state" of the source.

3.3. Width of the run-wise flux distribution

In order to determine if the measured width of the flux distribution (left panel of Fig. 3) can be explained as statistical fluctuations from the measurement process a simulation has been carried out considering a source that emits an integral flux above 200 GeV of 4.32×10^{-11} cm^{-2} s^{-1} with a power-law spectral index $\Gamma = 3.53$ (as determined in the next section). For each run of the data set D_{QS} the number n_γ expected by convolving the assumed differential energy spectrum with the instrument response corresponding to the observation conditions is determined. A random smearing around this value allows statistical fluctuations to be taken into account. The number of events in the off-source region and also the number of background events in the source region are derived from the measured values n_{off} in the data set. These are also smeared in order to take into account the expected statistical fluctuations.

10 000 such flux distributions have been simulated, and for each one its mean value and rms (which will be called below RMSD) are determined. The distribution of RMSD thus obtained, shown in Fig. 4, is well described by a Gaussian centred on 0.98×10^{-11} cm^{-2} s^{-1} (which represents a relative flux dispersion of 23%) and with a σ_{RMSD} of 0.07×10^{-11} cm^{-2} s^{-1}.

It should be noted that here the effect of atmospheric fluctuations in the determination of the flux is only taken into account at the level of the off-source events, as these numbers are taken from the measured data. But the effect of the corresponding level of fluctuations on the source signal is very difficult to determine. If a conservative value of 20% is considered[2] that is added in the simulations as a supplementary fluctuation factor for the number of events expected from the source, a RMSD distribution centred on 1.30×10^{-11} cm^{-2} s^{-1} with a σ_{RMSD} of 0.09×10^{-11} cm^{-2} s^{-1} is obtained. Even in this conservative case, the measured value for the flux distribution rms ($(2.48 \pm 0.11_{stat}) \times 10^{-11}$ cm^{-2} s^{-1}) is very far (more than 8 standard deviations) from the simulated value. All these elements strongly suggest the existence of an intrinsic variability associated with the quiescent state of PKS 2155−304.

[2] A similar procedure has been carried out on the Crab Nebula observations. Assuming this source is perfectly stable, it allows the derivation of an upper limit to the fluctuations of the Crab signal due to the atmosphere. Nonetheless, this value, ∼10%, is linked to the observations' epoch and zenith angles, and to the source spectral shape.

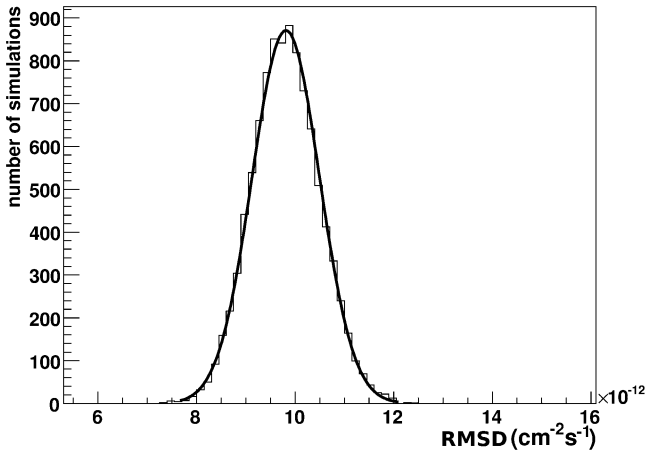

Fig. 4. Distribution of RMSD obtained when the instrument response to a fixed emission ($\Phi = 4.32 \times 10^{-11}$ cm^{-2} s^{-1} and $\Gamma = 3.53$) is simulated 10 000 times with the same observation conditions as for the 115 runs of the left part of Fig. 3.

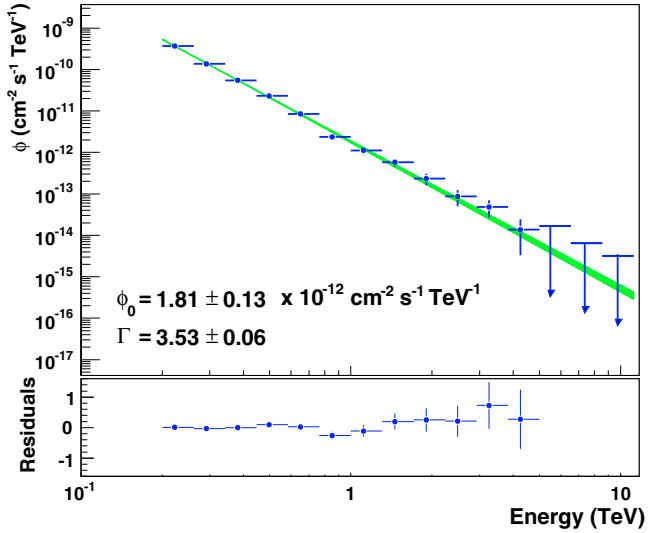

Fig. 5. Energy spectrum of the quiescent state for the period 2005–2007. The green band correponds to the 68% confidence-level provided by the maximum likelihood method. Points are derived from the residuals in each energy bin, only for illustration purposes. See Sect. 3.4 for further details.

3.4. Quiescent-state energy spectrum

The energy spectrum associated with the data set D_{QS}, shown in Fig. 5, is well described by a power law with a differential flux at 1 TeV of $\phi_0 = (1.81 \pm 0.13_{stat}) \times 10^{-12}$ cm^{-2} s^{-1} TeV^{-1} and an index of $\Gamma = 3.53 \pm 0.06_{stat}$. The stability of these values for spectra measured separately for 2005, 2006 (excluding July), and 2007 is presented in Table 5. The corresponding average integral flux is $(4.23 \pm 0.09_{stat}) \times 10^{-11}$ cm^{-2} s^{-1}, which is as expected in very good agreement with the mean value of the distribution shown in the left panel of Fig. 3.

Bins above 2 TeV correspond to γ−ray excesses lower than 20 γ and significances lower than 2σ. Above 5 TeV excesses are even less significant (∼1σ or less) and 99% upper-limits are

Table 5. Parametrization of the differential energy spectrum of the quiescent state of PKS 2155−304, determined in the energy range 0.2−10 TeV, first for the 2005–2007 period and also separately for the 2005, 2006 (excluding July) and 2007 periods.

Year	Data set	ϕ_0	Γ	Φ
2005–2007	$D_{\rm QS}$	1.81 ± 0.13	3.53 ± 0.06	4.23 ± 0.09
2005	$D_{\rm QS-2005}$	1.59 ± 0.32	3.56 ± 0.16	3.83 ± 0.21
2006	$D_{\rm QS-2006}$	1.87 ± 0.18	3.59 ± 0.08	4.65 ± 0.13
2007	$D_{\rm QS-2007}$	1.84 ± 0.24	3.43 ± 0.11	3.78 ± 0.16

Notes. Corresponding data sets are those of Table 2. ϕ_0 (10^{-12} cm^{-2} s^{-1} TeV^{-1}) is the differential flux at 1 TeV, Γ the photon index and Φ (10^{-11} cm^{-2} s^{-1}) the integral flux above 0.2 TeV. Errors are statistical.

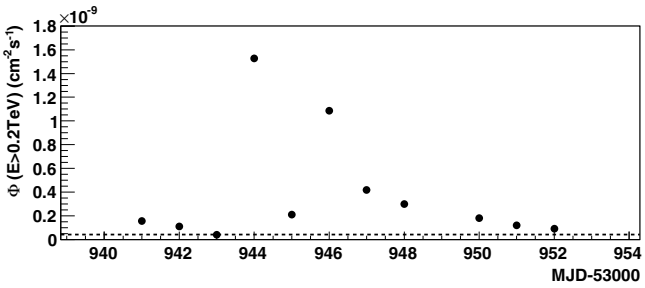

Fig. 6. Integral flux above 200 GeV measured each night during late July 2006 observations. The horizontal dashed line corresponds to the quiescent state emission level defined in Sect. 3.2.

used. There is no improvement of the fit when a curvature is taken into account.

4. Spectral variability

4.1. Variation of the spectral index for the whole data set 2005–2007

The spectral state of PKS 2155−304 has been monitored since 2002. The first set of observations (Aharonian et al. 2005b), from July 2002 to September 2003, shows an average energy spectrum well described by a power law with an index of $\Gamma = 3.32 \pm 0.06_{\rm stat}$, for an integral flux (extrapolated down to 200 GeV) of $(4.39 \pm 0.40_{\rm stat}) \times 10^{-11}$ cm^{-2} s^{-1}. No clear indication of spectral variability was seen. Consecutive observations in October and November 2003 (Aharonian et al. 2005c) gave a similar value for the index, $\Gamma = 3.37 \pm 0.07_{\rm stat}$, for a slightly higher flux of $(5.22 \pm 0.54_{\rm stat}) \times 10^{-11}$ cm^{-2} s^{-1}. Later, during HESS observations of the first (MJD 53944, Aharonian et al. 2007a) and second (MJD 53946, Aharonian et al. 2009) exceptional flares of July 2006, the source reached much higher average fluxes, corresponding to $(1.72 \pm 0.05_{\rm stat}) \times 10^{-9}$ cm^{-2} s^{-1} and $(1.24 \pm 0.02_{\rm stat}) \times 10^{-9}$ cm^{-2} s^{-1}[3] respectively. In the first case, no strong indications for spectral variability were found and the average index $\Gamma = 3.19 \pm 0.02_{\rm stat}$ was close to those associated with the 2002 and 2003 observations. In the second case, clear evidence of spectral hardening with increasing flux was found.

The observations of PKS 2155−304 presented in this paper also include the subsequent flares of 2006 and the data of 2005 and 2007. Therefore, the evolution of the spectral index is studied for the first time for a flux level varying over two orders of magnitude. This spectral study has been carried out over the fixed energy range 0.2−1 TeV in order to minimize both systematic effects due to the energy threshold variation and the effect of the curvature observed at high energy in the flaring states. The maximal energy has been chosen to be at the limit where the spectral curvature seen in high flux states begins to render the power law or exponential curvature hypotheses distinguishable. As flux levels observed in July 2006 are significantly higher than in the rest of the data set (see Fig. 6), the flux-index behavior is determined separately first for the July 2006 data set itself ($D_{\rm JULY06}$) and secondly for the 2005-2007 data excluding this data set ($D_{\rm QS}$).

On both data sets, the following method was applied. The integral flux was determined for each run assuming a power law shape with an index of $\Gamma = 3.37$ (average spectral index for the whole data set), and runs were sorted by increasing flux. The set of ordered runs was then divided into subsets containing at least an excess of 1500 γ above 200 GeV and the energy spectrum of each subset was determined[4].

The left panel of Fig. 7 shows the photon index versus integral flux for data sets $D_{\rm QS}$ (grey crosses) and $D_{\rm JULY06}$ (black points). Corresponding numbers are summarized in Appendix B. While a clear hardening is observed for integral fluxes above a few 10^{-10} cm^{-2} s^{-1}, a break in this behavior is observed for lower fluxes. Indeed, for the data set $D_{\rm JULY06}$ (black points) a linear fit yields a slope $d\Gamma/d\Phi = (3.0 \pm 0.3_{\rm stat}) \times 10^8$ cm^2 s, whereas the same fit for data set $D_{\rm QS}$ (grey crosses) yields a slope $d\Gamma/d\Phi = (-3.4 \pm 1.9_{\rm stat}) \times 10^9$ cm^2 s. The latter corresponds to a χ^2 probability $P(\chi^2) = 71\%$; a fit to a constant yields $P(\chi^2) = 33\%$ but with a constant fitted index incompatible with a linear extrapolation from higher flux states at a 3σ level. This is compatible with conclusions obtained either with an independent analysis or when these spectra are processed following a different prescription. In this prescription the runs were sorted as a function of time in contiguous subsets with similar photon statistics, rather than as a function of increasing flux.

The form of the relation between the index versus integral flux is unprecedented in the TeV regime. Prior to the results presented here, spectral variability has been detected only in two other blazars, Mrk 421 and Mrk 501. For Mrk 421, a clear hardening with increasing flux appeared during the 1999/2000 and 2000/2001 observations performed with HEGRA (Aharonian et al. 2002) and also during the 2004 observations performed with HESS (Aharonian et al. 2005a). In addition, the Mrk 501 observations carried out with CAT during the strong flares of 1997 (Djannati-Ataï et al. 1999) and also the recent observation performed by MAGIC in 2005 (Albert et al. 2007) have shown a similar hardening. In both studies, the VHE peak has been observed in the νF_ν distributions of the flaring states of Mrk 501.

4.2. Variation of the spectral index for the four flaring nights of July 2006

In this section, the spectral variability during the flares of July 2006 is described in more detail. A zoom on the variation of the integral flux (4-min binning) for the four nights containing the flares (nights MJD 53944, 53945, 53946, and 53947, called the "flaring period") is presented in the top panel of Fig. 8. This figure shows two exceptional peaks on MJD 53944 and MJD 53946 that climax respectively at fluxes higher than 2.5×10^{-9} cm^{-2} s^{-1} and 3.5×10^{-9} cm^{-2} s^{-1} (~9 and ~12 times the

[3] Corresponding to data set T200 in Aharonian et al. (2009).

[4] Even for lower fluxes, the significance associated with each subset is always higher than 20 standard deviations.

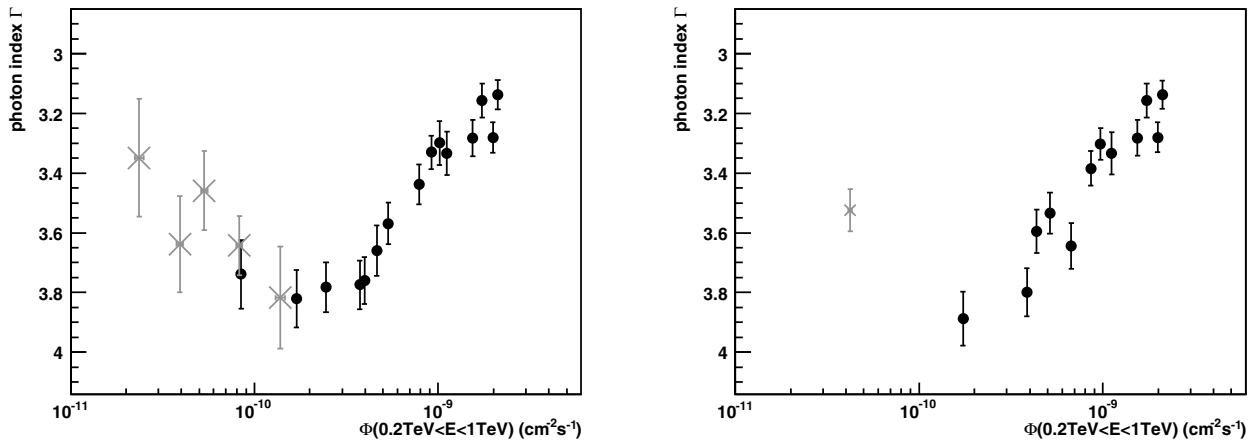

Fig. 7. Evolution of the photon index Γ with increasing flux Φ in the 0.2−1 TeV energy range. *The left panel* shows the results for the July 2006 data (black points, data set D_{JULY06}) and for the 2005−2007 period excluding July 2006 (grey points, data set D_{QS}). *The right panel* shows the results for the four nights flaring period of July 2006 (black points, data set D_{FLARES}) and one point corresponding to the quiescent state average spectrum (grey point, again data set D_{QS}). See text in Sects. 4.1 (*left panel*) and 4.2 (*right panel*) for further details on the method.

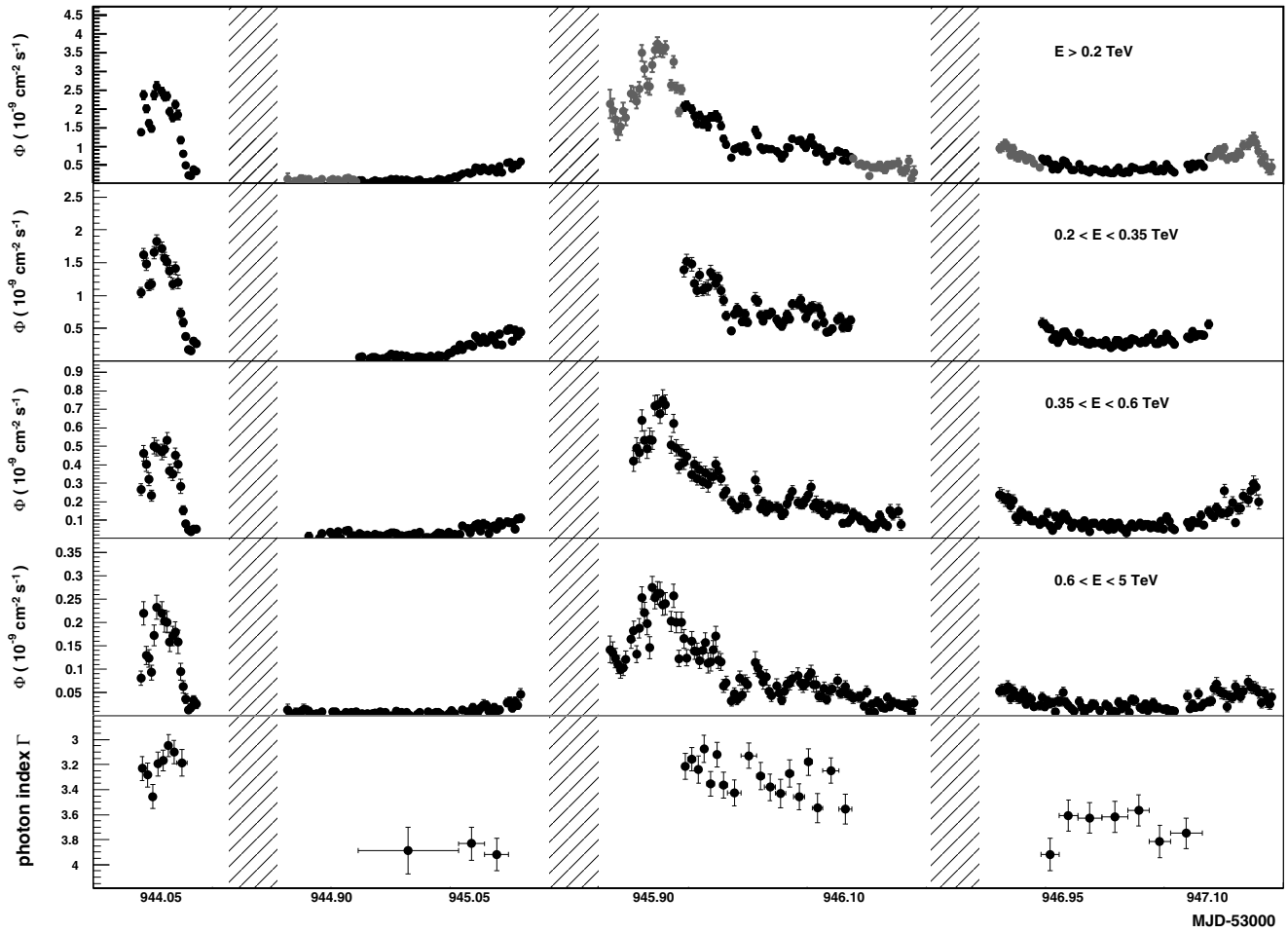

Fig. 8. Integrated flux versus time for PKS 2155−304 on MJD 53944–53947 for four energy bands and with a 4-min binning. *From top to bottom*: >0.2 TeV, 0.2–0.35 TeV, 0.35–0.6 TeV and 0.6–5 TeV. These light curves are obtained using a power law spectral shape with an index of $\Gamma = 3.37$, also used to derive the flux extrapolation down to 0.2 TeV when the threshold is above that energy in *the top panel* (grey points). Because of the high dispersion of the energy threshold of the instrument (see Sect. 2, Fig. 1), and following the prescription described in 3.1, the integral flux has been determined for a time bin only if the corresponding energy threshold is lower than E_{min}. The fractional rms for the light curves are respectively, $0.86 \pm 0.01_{\mathrm{stat}}$, $0.79 \pm 0.01_{\mathrm{stat}}$, $0.89 \pm 0.01_{\mathrm{stat}}$ and $1.01 \pm 0.02_{\mathrm{stat}}$. The last plot shows the variation of the photon index determined in the 0.2−1 TeV range. See Sect. 4.2 and Appendix B.4 for details.

Crab Nebula level above the same energy), both about two orders of magnitude above the quiescent state level.

The variation with time of the photon index is shown in the bottom panel of Fig. 8. To obtain these values, the γ excess

above 200 GeV has been determined for each 4-min bin. Then, successive bins have been grouped in order to reach a global excess higher than 600 γ. Finally, the energy spectrum of each data set has been determined in the 0.2−1 TeV energy range, as before (corresponding numbers are summarized in Appendix Table B.4). There is no clear indication of spectral variability within each night, except for MJD 53946 as shown in Aharonian et al. (2009). However, a variability can be seen from night to night, and the spectral hardening with increasing flux level already shown in Fig. 7 is also seen very clearly in this manner.

It is certainly interesting to directly compare the spectral behavior seen during the flaring period with the hardness of the energy spectrum associated with the quiescent state. This is shown in the right panel of Fig. 7, where black points correspond to the four flaring nights; these were determined in the same manner as for the left panel (see 4.1 for details). A linear fit here yields a slope $d\Gamma/d\Phi = (2.8 \pm 0.3_{stat}) \times 10^8$ cm^2 s. The grey cross corresponds to the integral flux and the photon index associated with the quiescent state (derived in a consistent way in the energy range from 0.2−1 TeV), showing a clear rupture with the tendancy at higher fluxes (typically above 10^{-10} cm^{-2} s^{-1}).

These four nights were further examined to search for differences in the spectral behavior between periods in which the source flux was clearly increasing and periods in which it was decreasing. For this, the first 16 min of the first flare (MJD 53944) are of special interest because they present a very symmetric situation: the flux increases during the first half, and then decreases to its initial level. The averaged fluxes are similar in both parts ($\sim 1.8 \times 10^{-9}$ cm^{-2} s^{-1}), and the observation conditions (and thus the instrument response) are almost constant – the mean zenith angle of each part being respectively 7.2 and 7.8 degrees. Again, the spectra have been determined in the 0.2−1 TeV energy range, giving indices of $\Gamma = 3.27 \pm 0.12_{stat}$ and $\Gamma = 3.27 \pm 0.09_{stat}$ respectively. To further investigate this question and avoid potential systematic errors from the spectral method determination, the hardness ratios were derived (defined as the ratio of the excesses in different energy bands), using for this the energy (TeV) bands [0.2−0.35], [0.35−0.6] and [0.6−5.0]. For any combination, no differences were found beyond the 1σ level between the increasing and decreasing parts. A similar approach has been applied – when possible – for the rest of the flaring period. No clear dependence has been found within the statistical error limit of the determined indices, which is distributed between 0.09 and 0.20.

Finally, the persistence of the energy cut-off in the differential energy spectrum along the flaring period has been examined. For this purpose, runs were sorted again by increasing flux and grouped into subsets containing at least an excess of 3000 γ above 200 GeV[5]. For the seven subsets found, the energy spectrum has been determined in the 0.2−10 TeV energy range both for a simple power law and a power law with an exponential cut-off. This last hypothesis was found to be favoured systematically at a level varying from 1.8 to 4.6σ compared to the simple power law and is always compatible with a cut-off in the 1−2 TeV range.

5. Light curve variability and correlation studies

This section is devoted to the characterization of the temporal variability of PKS 2155−304, focusing on the flaring period observations. The high number of γ-rays available not only enabled minute-level time scale studies, such as those presented for MJD 53944 in Aharonian et al. (2007a), but also to derive detailed light curves for three energy bands (Fig. 8): 0.2−0.35 TeV, 0.35−0.6 TeV and 0.6−5 TeV.

The variability of the energy-dependent light curves of PKS 2155−304 is in the following quantified through their fractional rms F_{var} defined in Eq. (4) (Nandra et al. 1997; Edelson et al. 2002). In addition, possible time lags between light curves in two energy bands are investigated.

5.1. Fractional rms F_{var}

All fluxes in the energy bands of Fig. 8 show a strong variability that is quantified through their fractional rms F_{var} (which depends on observation durations and their sampling). Measurement errors $\sigma_{i,err}$ on each of the N fluxes ϕ_i of the light curve are taken into account in the definition of F_{var}:

$$F_{var} = \frac{\sqrt{S^2 - \sigma_{err}^2}}{\overline{\phi}} \tag{4}$$

where S^2 is the variance

$$S^2 = \frac{1}{N-1} \sum_{i=1}^{N} (\phi_i - \overline{\phi})^2, \tag{5}$$

and where σ_{err}^2 is the mean square error and $\overline{\phi}$ is the mean flux.

The energy-dependent variability $F_{var}(E)$ has been calculated for the flaring period according to Eq. (4) in all three energy bands. The uncertainties on $F_{var}(E)$ have been estimated according to the parametrization derived by Vaughan et al. (2003b), using a Monte Carlo approach which accounts for the measurement errors on the simulated light curves.

Figure 9 shows the energy dependence of F_{var} over the four nights for a sampling of 4 min where only fluxes with a significance of at least 2 standard deviations were considered. There is a clear energy-dependence of the variability (a null probability of $\sim 10^{-16}$). The points in Fig. 9 are fitted according to a power law showing that the variability follows $F_{var}(E) \propto E^{0.19 \pm 0.01}$.

This energy dependence of F_{var} is also perceptible within each individual night. In Table 6 the values of F_{var}, the relative mean flux and the observation duration, are reported night by night for the flaring period. Because of the steeply falling spectra, the low-energy events dominate in the light curves. This lack of statistics for high energy prevents to have a high fraction of points with a significance more than 2 standard deviation in light curves night by night for the three energy bands previously considered. On the other hand, the error contribution dominates, preventing the estimation of the F_{var} in all these three energy bands. Therefore, only two energy bands were considered: low (0.2−0.5 TeV) and high (0.5−5 TeV). As can be seen in Table 6 also night by night the high-energy fluxes seem to be more variable than those at lower energies.

5.2. Doubling/halving timescale

While F_{var} characterizes the mean variability of a source, the shortest doubling/halving time (Zhang et al. 1999) is an important parameter in view of finding an upper limit on a possible physical shortest time scale of the blazar.

If Φ_i represents the light curve flux at a time T_i, for each pair of Φ_i one may calculate $T_2^{i,j} = |\Phi \Delta T / \Delta \Phi|$, where $\Delta T = T_j - T_i$,

[5] To be significant, the determination of an energy cut-off needs a higher number of γ than for a power-law fit.

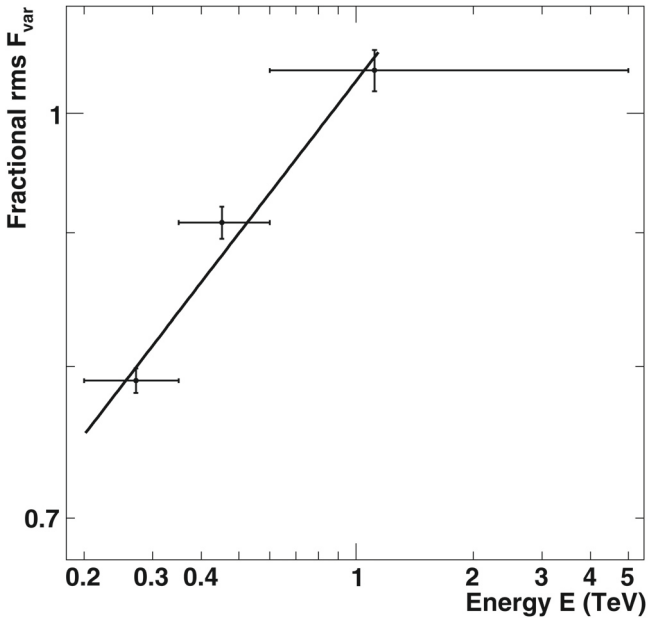

Fig. 9. Fractional rms F_{var} versus energy for the observation period MJD 53944–53947. The points are the mean value of the energy in the range represented by the horizontal bars. The line is the result of a power law fit where the errors on F_{var} and on the mean energy are taken into account, yielding $F_{var}(E) \propto E^{0.19\pm0.01}$.

Table 6. Mean Flux and the fractional rms F_{var} night by night for MJD 53944–53947.

MJD	Duration (min)	Energy (TeV)	$\overline{\Phi}$ (10^{-10} cm^{-2} s^{-1})	F_{var}
53944	88			
		all	15.44 ± 0.87	0.56 ± 0.01
		0.2–0.5	13.28 ± 0.85	0.55 ± 0.01
		0.5–5.0	1.94 ± 0.24	0.61 ± 0.03
53945	244			
		all	2.40 ± 0.41	0.67 ± 0.03
		0.2–0.5	2.35 ± 0.42	0.64 ± 0.03
		0.5–5.0	0.34 ± 0.12	–
53946	252			
		all	11.39 ± 0.80	0.35 ± 0.01
		0.2–0.5	10.02 ± 0.79	0.33 ± 0.01
		0.5–5.0	1.39 ± 0.20	0.43 ± 0.02
53947	252			
		all	4.26 ± 0.52	0.22 ± 0.02
		0.2–0.5	4.02 ± 0.52	0.22 ± 0.02
		0.5–5.0	0.37 ± 0.11	0.13 ± 0.09

Notes. The values refers to light curves with 4 min bins and respectively in three energy bands: >0.2 TeV, 0.2−0.5 TeV, 0.5−5.0 TeV. Since a significant fraction (≈40%) of the points in the light curve of MJD 53945 in the energy band 0.5−5.0 TeV have a significance of less than 2 standard deviations, its F_{var} is not estimated.

$\Delta\Phi = \Phi_j - \Phi_i$ and $\Phi = (\Phi_j + \Phi_i)/2$. Two possible definitions of the doubling/halving are proposed by Zhang et al. (1999): the smallest doubling time of all data pairs in a light curve (T_2), or the mean of the 5 smallest $T_2^{i,j}$ (in the following indicated as $\tilde{T}_2$). One should keep in mind that, according to Zhang et al. (1999), these quantities are ill defined and strongly depend on the length of the sampling intervals and on the signal-to-noise ratio in the observation.

Table 7. Doubling/Halving times for the high intensity nights MJD 53944 and MJD 53946 estimated with two different samplings, using the two definitions explained in the text.

MJD	Bin size	T_2[min]	$\tilde{T}_2$[min]	Fraction of pairs
53944	1 min	1.65 ± 0.38	2.27 ± 0.77	0.53
53944	2 min	2.20 ± 0.60	4.45 ± 1.64	0.62
53946	1 min	1.61 ± 0.45	5.72 ± 3.83	0.25
53946	2 min	4.55 ± 1.19	9.15 ± 4.05	0.38

Notes. The final column corresponds to the fraction of flux pairs kept to estimate the doubling times.

This quantity was calculated for the two nights with the highest fluxes, MJD 53944 and MJD 53946, considering light curves with two different binnings (1 and 2 min). Bins with flux significances more than 2σ and flux ratios with an uncertainty smaller than 30% were required to estimate the doubling time scale. The uncertainty on T_2 was estimated by propagating the errors on the Φ_i, and a dispersion of the 5 smallest values was included in the error for $\tilde{T}_2$.

In Table 7, the values of T_2 and $\tilde{T}_2$ for the two nights are shown. The dependence with respect to the binning is clearly visible for both observables. In this table, the last column shows that the fraction of pairs in the light curves that are kept in order to estimate the doubling times is on average ∼45%. Moreover, doubling times T_2 and $\tilde{T}_2$ have been estimated for two sets of pairs in the light curves where $\Delta\Phi = \Phi_j - \Phi_i$ is increasing or decreasing respectively. The values of the doubling time for the two cases are compatible within 1σ, therefore no significant asymmetry has been found.

It should be noted that these values are strongly dependent on the time binning and on the experiment's sensitivity, so that the typical fastest doubling timescale should be conservatively estimated as being less than ∼2 min, which is compatible with the values reported in Aharonian et al. (2007a) and in Albert et al. (2007), the latter concerning the blazar Mrk 501.

5.3. Cross-correlation analysis as a function of energy

Time lags between light curves at different energies can provide insight into acceleration, cooling and propagation effects of the radiative particles.

The discrete correlation function (DCF) as a function of the delay (White & Peterson 1984; Edelson & Krolik 1988) is used here to search for possible time lags between the energy-resolved light curves. The uncertainty on the DCF has been estimated using simulations. For each delay, 10^5 light curves (in both energy bands) have been generated within their errors, assuming a Gaussian probability distribution. A probability distribution function (PDF) of the correlation coefficients between the two energy bands has been estimated for each set of simulated light curves. The rms of these PDF are the errors related to the DCF at each delay. Figure 10 shows the DCF between the high and low-energy bands for the four-night flaring period (with 4 min bins) and for the second flaring night (with 2 min bins). The gaps between each 28 min run have been taken into account in the DCF estimation.

The position of the maximum of the DCF has been estimated by a Gaussian fit that shows no time lag between low and high energies for either the 4 or 2 min binned light curves. This sets a limit of 14 ± 41 s from the observation of MJD 53946. A detailed study on the limit on the energy scale on which quantum

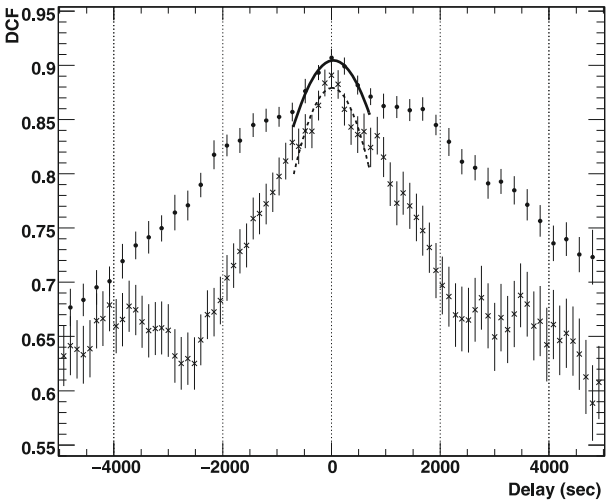

Fig. 10. DCF between the light curves in the energy ranges 0.2−0.5 TeV and 0.5−5 TeV and Gaussian fits around the peak. Full circles represent the DCF for MJD 53944–53947 4-min light curve and the solid line is the Gaussian fit around the peak with mean value of 43 ± 51 s. Crosses represent the DCF for MJD 53946 with a 2-min light curve binning, and the dashed line in the Gaussian fit with a peak centred at 14 ± 41 s.

gravity effects could become important, using the same data set, are reported in Aharonian et al. (2008a).

5.4. Excess rms-flux correlation

Having defined the shortest variability time scales, the nature of the process that generates the fluctuations is investigated, using another estimator: the excess rms. It is defined as the variance of a light curve (Eq. (5)) after subtracting the measurement error:

$$\sigma_{\rm xs} = \sqrt{(S^2 - \sigma_{\rm err}^2)}. \quad (6)$$

Figure 11 shows the correlation between the excess rms of the light curve and the flux, where the flux here considered are selected with an energy threshold of 200 GeV. The excess variance is estimated for 1- and 4-min binned light curves, using 20 consecutive flux points Φ_i that are at least at the 2σ significance level (81% of the 1 min binned sample). The correlation factors are $r_1 = 0.60^{+0.21}_{-0.25}$ and $r_4 = 0.87^{+0.10}_{-0.24}$ for the 1 and 4 min binning, excluding an absence of correlation at the 2σ and 4σ levels respectively, implying that fluctuations in the flux are probably proportional to the flux itself, which is a characteristic of lognormal distributions (Aitchinson & Brown 1963). This correlation has also been investigated extending the analysis to a statistically more significant data set including observations with a higher energy threshold in which the determination of the flux above 200 GeV requires an extrapolation (grey points in the top panel in Fig. 8). In this case the correlations found are compatible ($r_1 = 0.78^{+0.12}_{-0.14}$ and $r_4 = 0.93^{+0.05}_{-0.15}$ for the 1 and 4 min binning, respectively) and also exclude an absence of correlation with a higher significance (4σ and 7σ, respectively).

Such a correlation has already been observed for X-rays in the Seyfert class AGN (Edelson et al. 2002; Vaughan et al. 2003a,b; M$^{\rm c}$Hardy et al. 2004) and in X-ray binaries (Uttley & M$^{\rm c}$Hardy 2001; Uttley 2004; Gleissner et al. 2004), where it is considered as evidence for an underlying stochastic multiplicative process (Uttley et al. 2005), as opposed to an additive process. In additive processes, light curves are considered as the sum of individual flares "shots" contributing from several zones (multi-zone models) and the relevant variable that has a Gaussian distribution (namely Gaussian variable) is the flux. For multiplicative (or cascade) models the Gaussian variable is the logarithm of the flux. Therefore, this first observation of a strong rms-flux correlation in the VHE domain fully confirms the lognormality of the flux distribution presented in Sect. 3.2.

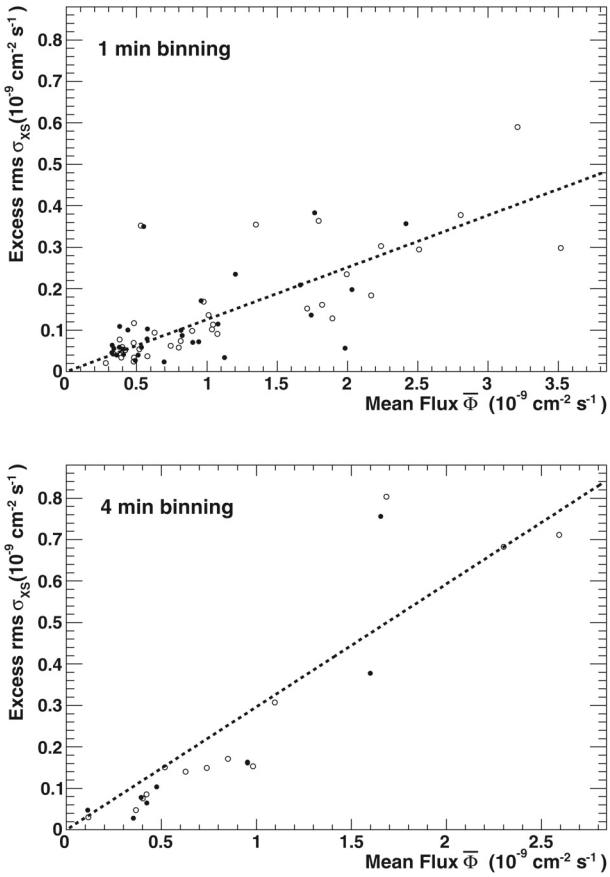

Fig. 11. The excess rms $\sigma_{\rm xs}$ vs. mean flux $\bar{\Phi}$ for the observation in MJD 53944–53947 (Full circles). The open circles are the additional points obtained when also including the extrapolated flux points – see text). *Top*: $\sigma_{\rm xs}$ estimated with 20 min time intervals and a 1 min binned light curve. *Bottom*: $\sigma_{\rm xs}$ estimated with 80 min time intervals and a 4 min binned light curve. The dotted lines are a linear fit to the points, where $\sigma_{\rm xs} \propto 0.13 \times \bar{\Phi}$ for the 1 min binning and $\sigma_{\rm xs} \propto 0.3 \times \bar{\Phi}$ for the 4 min binning. Fits to the open circles yield similar results.

6. Characterization of the lognormal process during the flaring period

This section investigates whether the variability of PKS 2155−304 in the flaring period can be described by a random stationary process, where, as shown in Sect. 5.4, the Gaussian variable is the logarithm of the flux. In this case the variability can be characterized through its Power Spectral Density (PSD) (van der Klis 1997), which indicates the density of variance as function of the frequency ν. The PSD is an intrinsic indicator of the variability, usually represented in large frequency intervals by power laws ($\propto \nu^{-\alpha}$) and is often used to define different "states" of variable objects (see e.g., Paltani et al. 1997; and Zhang et al. 1999, for the PSD of PKS 2155−304 in the optical and X-rays). The PSD of the light curve of one single night (MJD 53944) was given in Aharonian et al. (2007a) between 10^{-4} and 10^{-2} Hz, and was found to be compatible

with a red noise process ($\alpha \geq 2$) with ~10 times more power as in archival X-ray data (Zhang et al. 1999), but with a similar index. This study implicitely assumed the γ-ray flux to be the Gaussian variable. In the present paper, the PSD is determined using data from 4 consecutive nights (MJD 53944–53947) and assuming a lognormal process. Since direct Fourier analysis is not well adapted to light curves extending over multiple days and affected by uneven sampling and uneven flux errors, the PSD will be further determined on the basis of parametric estimation and simulations.

In the hypothesis where the process is stationary, i.e., the PSD is time-independent, a power-law shape of the PSD was assumed, as for X-ray emitting blazars. The PSD was defined as depending on two parameters and as follows: $P(\nu) = K(\nu_{\rm ref}/\nu)^{\alpha}$, where α is the variability spectral index and K denotes the "power" (i.e., the variance density) at a reference frequency $\nu_{\rm ref}$. This latter was conventionally chosen to be 10^{-4} Hz, where the two parameters α and K are found to be decorrelated. Since a lognormal process is considered, $P(\nu)$ is the density of variance of the Gaussian variable $\ln \Phi$. The *natural* logarithm of the flux is conveniently used here, since its variance over a given frequency interval[6] is close to the corresponding value of $F_{\rm var}^2$, at least for small fluctuations. For a given set of α and K, it is possible to simulate many long time series and to modify them according to experimental effects, namely those of background events and of flux measurement errors. Light curve segments are further extracted from this simulation, with exactly the same time structure (observation and non-observation intervals) and the same sampling rates as those of real data. The distributions of several observables obtained from simulations for different values of α and K will be compared to those determined from observations, thus allowing these parameters to be determined from a maximum-likelihood fit.

The simulation characteristics will be described in Sect. 6.1. Sections 6.2–6.4 will be devoted to the determination of α and K by three methods, each of them based on an experimental result: the excess rms-flux correlation, the Kolmogorov first-order structure function (Rutman 1978; Simonetti et al. 1985) and doubling-time measurements.

6.1. Simulation of realistic time-series

For practical reasons, simulated values of $\ln \Phi$ were calculated from Fourier series, thus with a discrete PSD. The fundamental frequency $\nu_0 = 1/T_0$ that corresponds to an elementary bin $\delta\nu \equiv \nu_0$ in frequency, must be much lower than $1/T$ if T is the duration of the observation. The ratio T_0/T was chosen to be of the order of 100, in such a way that the influence of a finite value of T_0 on the average variance of a light curve of duration T would be less than about 2%. Taking $T_0 = 9 \times 10^5$ s, this condition is fulfilled for the following studies. With this approximation, the simulated flux logarithms are given by:

$$\ln \Phi(t) = a_0 + \sum_{n=1}^{N_{\rm max}} a_n \cos(2n\pi\nu_0 t + \varphi_n) \qquad (7)$$

where $N_{\rm max}$ is chosen in such a way that $T_0/N_{\rm max}$ is less than the time interval between consecutive measurements (i.e., the sampling interval). According to the definition of a Gaussian random process, the phases φ_n are uniformly distributed between 0 and 2π and the Fourier coefficients a_n are normally distributed with mean 0 and variances given by $P(\nu)\,\delta\nu/2$ with $\nu = n\,\delta\nu = n\,\nu_0$.

From the long simulated time-series, light curve segments were extracted with the same durations as the periods of continuous data taking and with the same gaps between them. The simulated fluxes were further smeared according to measurement errors, according to the observing conditions (essentially zenith angle and background rate effects) in the corresponding data set.

[6] If σ^2 is the variance of $\ln \Phi$, $F_{\rm var} = \sqrt{\exp(\sigma^2) - 1}$.

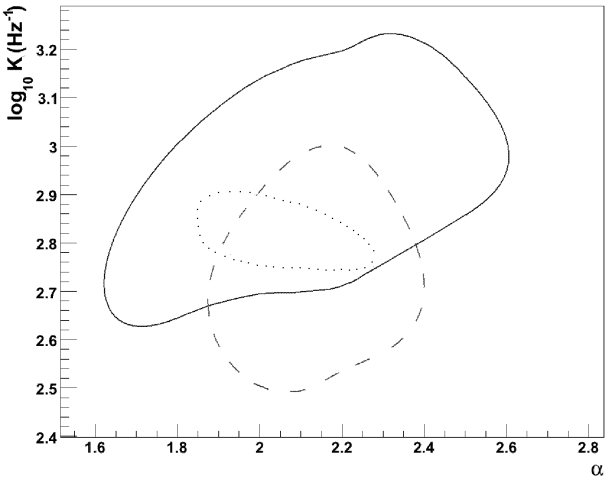

Fig. 12. 95% confidence domains for α and K at $\nu_{\rm ref} = 10^{-4}$ Hz obtained by a maximum-likelihood method based on the $\sigma_{\rm xs}$-flux correlation from 500 simulated light curves. The dashed contour refers to light curve segments of 20 min duration, sampled every minute. The solid contour refers to light curve segments of 80 min duration, sampled every 4 min. The dotted contour refers to the method based on the structure function, as explained in Sect. 6.3.

6.2. Characterization of the lognormal process by the excess rms-flux relation

For a fixed PSD, characterized by a set of parameters $\{\alpha, K\}$, 500 light curves were simulated, reproducing the observing conditions of the flaring period (MJD 53944–53947), according to the procedure explained in Sect. 6.1.

For each set of simulated light curves, segments of 20 min duration sampled every minute (and alternatively segments of 80 min duration sampled every 4 min) were extracted and, for each of them, the excess rms $\sigma_{\rm xs}$ and the mean flux $\bar{\Phi}$ were calculated as explained in Sect. 5.4. For a wide range of values of α and K, simulated light curves reproduce well the high level of correlation found in the measured light curves. On the other hand, the fractional variability $F_{\rm var}$ and $\bar{\Phi}$ are essentially uncorrelated and will be used in the following. A likelihood function of α and K was obtained by comparing the simulated distributions of $F_{\rm var}$ and $\bar{\Phi}$ to the experimental ones. An additional observable that is sensitive to α and K is the fraction of those light curve segments for which $F_{\rm var}$ cannot be calculated because large measurement errors lead to a negative value for the excess variance. The comparison between the measured value of this fraction and those obtained from simulations is also taken into account in the likelihood function. The 95% confidence contours for the two parameters α and K obtained from the maximum likelihood method are shown in Fig. 12 for both kinds of light curve segments. The two selected domains in the $\{\alpha, K\}$ plane have a large overlap which restricts the values of α to the interval (1.9, 2.4).

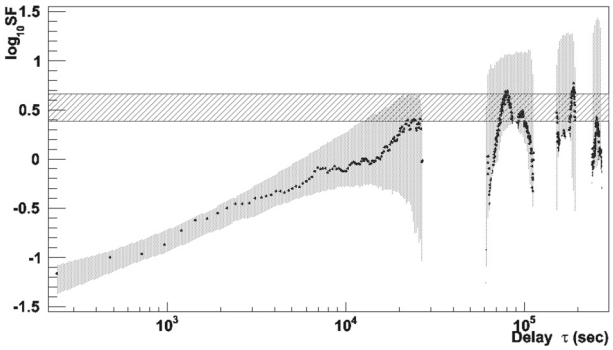

Fig. 13. First order structure function SF for the observations carried out in the period MJD 53944–53947 (circles). The shaded area corresponds to the 68% confidence limits obtained from simulations for the lognormal stationary process characterized by $\alpha = 2$ and $\log_{10}(K/\mathrm{Hz}^{-1}) = 2.8$. The superimposed horizontal band represents the allowed range for the asymptotic value of the SF as obtained in Sect. 7.

6.3. Characterization of the lognormal process by the structure function analysis

Another method for determining α and K is based on Kolmogorov structure functions (SF). For a signal $X(t)$, measured at N pairs of times separated by a delay τ, $\{t_i, t_i + \tau\}$ $(i = 1, ..., N)$, the first-order structure function is defined as (Simonetti et al. 1985):

$$\begin{aligned} \mathrm{SF}(\tau) &= \frac{1}{N}\sum_{i=1}^{N}[X(t_i) - X(t_i+\tau)]^2 \\ &= \frac{1}{N}\sum_{i=1}^{N}[\ln\Phi(t_i) - \ln\Phi(t_i+\tau)]^2. \end{aligned} \quad (8)$$

In the present analysis, $X(t)$ represents the variable whose PSD is being estimated, namely $\ln\Phi$. The structure function is a powerful tool for studying aperiodic signals (Rutman 1978; Simonetti et al. 1985), such as the luminosity of blazars at various wavelengths. Compared to the direct Fourier analysis, the SF has the advantage of being less affected by "windowing effects" caused by large gaps between short observation periods in VHE observations. The first-order structure function is adapted to those PSDs whose variability spectral index is less than 3 (Rutman 1978), which is the case here, according to the results of the preceding section.

Figure 13 shows the first-order SF estimated for the flaring period (circles) for $\tau < 60$ h. At fixed τ, the distribution of $\mathrm{SF}(\tau)$ expected for a given set of parameters $\{\alpha, K\}$ is obtained from 500 simulated light curves. As an example, taking $\alpha = 2$ and $\log_{10}(K/\mathrm{Hz}^{-1}) = 2.8$, values of $\mathrm{SF}(\tau)$ are found to lie at 68% confidence level within the shaded region in Fig. 13.

In the case of a power law PSD with index α, the SF averaged over an ensemble of light curves is expected show a variation as $\tau^{\alpha-1}$ (Kataoka et al. 2001). However, this property does not take into account the effect of measurement errors, nor of the limited sensitivity of Cherenkov telescopes at lower fluxes. For the present study, it was preferable to use the distributions of $\mathrm{SF}(\tau)$ obtained from realistic simulations including all experimental effects. Using such distributions expected for a given set of parameters $\{\alpha, K\}$, a likelihood function can be obtained from the experimental SF and further maximized with respect to these two parameters. Furthermore, the likelihood fit was restricted to values of τ lower than 10^4 s, for which the expected fluctuations are not too large and are well-controlled. The 95% confidence region in the $\{\alpha, K\}$ plane thus obtained is indicated by the dotted line in Fig. 12. It is in very good agreement with those based on the excess rms-flux correlation and give the best values for α and K:

$$\alpha = 2.06 \pm 0.21 \quad \text{and} \quad \log_{10}(K/\mathrm{Hz}^{-1}) = 2.82 \pm 0.08. \quad (9)$$

The variability index α at VHE energies is found to be remarkably close to those measured in the X-ray domain on PKS 2155−304, Mrk 421, and Mrk 501 (Kataoka et al. 2001).

Table 8. Confidence interval at 68% c.l. for T_2 and $\tilde{T}_2$ predicted by simulations for $\alpha = 2$ and $\log_{10}(K/(\mathrm{Hz}^{-1})) = 2.8$ for the two high-intensity nights MJD 53944 and MJD 53946, with two different sampling intervals (1 and 2 min).

MJD	Bin size	T_2[min]	$\tilde{T}_2$[min]
53944	1 min	0.93–1.85	1.60–2.60
53944	2 min	3.01–4.28	4.52–6.40
53946	1 min	1.8–2.3	1.96–2.41
53946	2 min	5.3–9.1	6.6–12.1

6.4. Characterization of the lognormal process by doubling times

Simulations were also used to investigate if the estimator T_2 can be used to constrain the values of α and K. However, for α less than 2, no significant constraints on those parameters are obtained from the values of T_2. For higher values of α, doubling times only provide loose confidence intervals on K that are compatible with the values reported above. This can be seen in Table 8, showing the 68% confidence intervals predicted for T_2 and $\tilde{T}_2$ for a lognormal process with $\alpha = 2$ and $\log_{10}(K/(\mathrm{Hz}^{-1})) = 2.8$, as obtained from simulation. Therefore, the variability of PKS 2155−304 during the flaring period can be consistently described by the lognormal random process whose PSD is characterized by the parameters given by Eq. (9).

7. Limits on characteristic time of PKS 2155−304

In Sect. 5.2 the shortest variability time scale of PKS 2155−304 using estimators like doubling times have been estimated. This corresponds to exploring the high-frequency behavior of the PSD. In this section the lower ($<10^{-4}$ Hz) frequency part of the PSD will be considered, aiming to set a limit on the timescale above which the PSD, characterized in Sect. 6, starts to steepen to $\alpha > 2$. A break in the PSD is expected to avoid infrared divergences and the time at which this break occurs can be considered as a characteristic time, from which physical mechanisms occurring in AGN could be inferred.

Clearly the description of the source variability during the flaring period by a stationary lognormal random process is in good agreement with the flux distributions shown in Fig. 3. Considering the second Gaussian fit in the right panel of Fig. 3, the excess variance in the flaring regime reported in Table 9, although affected by a large error, is an estimator of the intrinsic variance of the stationary process. It has been demonstrated that $2\sigma_{\mathrm{xs}}^2$ represents the asymptotic value of the first-order structure function for large values of the delay τ (Simonetti et al. 1985). On the other hand, as already mentioned, a PSD proportional to $\nu^{-\alpha}$ with $\alpha \approx 2$ cannot be extrapolated to arbitrary low frequencies; equivalently, the average structure function cannot rise as $\tau^{\alpha-1}$ for arbitrarily long times. Therefore, by setting a 95% confidence interval on $\log_{10}\mathrm{SF}_{\mathrm{asympt}} = \log_{10}(2\sigma_{\mathrm{xs}}^2)$

Table 9. Variability estimators (definitions in Sect. 5.1) relative to $\ln\Phi$ both for the "quiescent" and flaring regime, as defined in Sect. 3.2.

	"Quiescent" regime	Flaring regime
$\sigma^2_{\rm exp}$ of $\ln\Phi$	0.304 ± 0.040	1.78 ± 0.27
$\sigma^2_{\rm err}$ of $\ln\Phi$	0.169 ± 0.053	0.022 ± 0.005
$\sigma^2_{\rm xs}$ of $\ln\Phi$	0.135 ± 0.067	1.758 ± 0.273

Notes. Experimental variance (line 1), error contribution to the variance (line 2), and excess variance (line 3). The latter is directly comparable to $F^2_{\rm var}$.

of $[0.38, 0.66]$ from Table 9, it is possible to evaluate a confidence interval on a timescale above which the average value of the structure function cannot be described by a power law. Taking account of the uncertainties on α and K given by Eq. (9), leads to the 95% confidence interval for this characteristic time $T_{\rm char}$ of the blazar in the flaring regime:

$$3\,{\rm h} < T_{\rm char} < 20\,{\rm h}.$$

This is compatible with the behavior of the experimental structure function at times $\tau > 10^4$ s (Fig. 13), although the large fluctuations expected in this region do not allow a more accurate estimation. In the X-ray domain, characteristic times of the order of one day or less have been found for several blazars including PKS 2155−304 (Kataoka et al. 2001). The results presented here suggest a strong similarity between the PSDs for X-rays and VHE γ-rays during flaring periods.

8. Discussion and conclusions

This data set, which exhibits unique features and results, is the outcome of a long-term monitoring program and dedicated, dense, observations. One of the main results here is the evidence for a VHE γ-ray quiescent-state emission, where the variations in the flux are found to have a lognormal distribution. The existence of such a state was postulated by Stecker & Salamon (1996) in order to explain the extragalactic γ-ray background at 0.03−100 GeV detected by EGRET (Fichtel 1996; Sreekumar et al. 1998) as coming from quiescent-state unresolved blazars. Such a background has not yet been detected in the VHE range, as it is technically difficult with the atmospheric Cherenkov technique to find an isotropic extragalactic emission and even more to distinguish it from the cosmic-ray electron flux (Aharonian et al. 2008b). In addition, the EBL attenuation limits the distance from which ∼TeV γ-rays can propagate to ∼1 Gpc (Aharonian et al. 2007b). As pointed out by Cheng et al. (2000), emission mechanisms might be simpler to understand during quiescent states in blazars, and they are also the most likely state to be found observationally. In the X-ray band, the existence of a steady underlying emission has also been invoked for two other VHE emitting blazars (Mrk 421, Fossati et al. 2000; and 1ES 1959+650, Giebels et al. 2002). Being able to separate, and detect, flaring and nonflaring states in VHE γ-rays is thus important for such studies.

The observation of the spectacular outbursts of PKS 2155–304 in July 2006 represents one of the most extreme examples of AGN variability in the TeV domain, and allows spectral and timing properties to be probed over two orders of magnitude in flux. For the flaring states a clear hardening of the spectrum with increasing flux above a few 10^{-10} cm^{-2} s^{-1} is observed, as was seen for the blazars Mrk 421 and Mrk 501. In contrast, for the quiescent state of PKS 2155−304 an indication of a softening is noted. If confirmed, this is a new and intruiging observation in the VHE regime of blazars. The blazar PKS 0208−512 (of the FSRQ class) also shows such initial softening and subsequent hardening with flux in the MeV range, but no general trend could be found for γ-ray blazars (Nandikotkur et al. 2007). In the framework of synchrotron self-Compton scenarios, VHE spectral softening with increasing flux can be associated with, for example, an increase in magnetic field intensity, emission region size, or the power law index of the underlying electron distribution, keeping all other parameters constant. A spectral hardening can equally be obtained by increasing the maximal Lorentz factor of the electron distribution or the Doppler factor (see e.g. Fig. 11.7 in Kataoka 1999). A better understanding of the mechanisms in play would require multi-wavelength observations to be taken over a similar time span and with similar sampling density as the data set presented here.

It is shown that the variability time scale $t_{\rm var}$ of a few minutes are only upper limits for the intrinsic lowest characteristic time scale. Doppler factors of $\delta \geq 100$ of the emission region are derived by Aharonian et al. (2007a) using the $\sim 10^9\ M_\odot$ black hole (BH) Schwarzschild radius light crossing time as a limit, while Begelman et al. (2008) argue that such fast time scales cannot be linked to the size of the BH and must occur in regions of smaller scales, such as "needles" of matter moving faster than average within a larger jet (Ghisellini & Tavecchio 2008), small components in the jet dominating at TeV energies (Katarzyński et al. 2008), or jet "stratification" (Boutelier et al. 2008). Levinson (2007) attributes the variability to dissipation in the jet coming from radiative deceleration of shells with high Lorentz factors.

The flaring period allowed the study of light curves in separated energy bands and the derivation of a power law dependence of $F_{\rm var}$ with the energy ($F_{\rm var} \propto E^{\sim 0.2}$). This dependence is comparable to that reported in Giebels et al. (2007), Lichti et al. (2008), Maraschi et al. (2002), where $F_{\rm var}(E) \propto E^{\sim 0.2}$ between the optical and X-ray energy bands was found for Mrk 421 and PKS 2155−304, respectively. An increase with the energy of the flux variability has been found for Mrk 501 (Albert et al. 2007) in VHE γ-rays on timescales comparable to those observed here.

The flaring period showed for the first time that the intrinsic variability of PKS 2155−304 increases with the flux, which can itself be described by a lognormal process, indicating that the aperiodic variability of PKS 2155−304 could be produced by a multiplicative process. The flux in the "quiescent regime", which is on average 50 times lower than in the flaring period and has a 3 times lower $F_{\rm var}$, also follows a lognormal distribution, suggesting similarities between these two regimes.

It has been possible to characterize a power spectral density of the flaring period in the frequency range 10^{-4}–10^{-2} Hz, resulting in a power law of index $\alpha = 2.06 \pm 0.21$ valid for frequencies down to ∼1/day. The description of the rapid variability of a TeV blazar as a random stationary process must be taken into account by time-dependent blazar models. For PKS 2155−304 the evidence of this log-normality has been found very recently in X-rays (Giebels & Degrange 2009) and as previously mentioned, X-ray binaries and Seyfert galaxies also show lognormal variability, which is thought to originate from the accretion disk (M$^{\rm c}$Hardy et al. 2004; Lyubarskii et al. 1997; Arévalo & Uttley 2006), suggesting a connection between the disk and the jet. This variability behavior should therefore be searched for in existing blazar light curves, independently of the observed wavelength.

Acknowledgements. The support of the Namibian authorities and of the University of Namibia in facilitating the construction and operation of HESS is

gratefully acknowledged, as is the support by the German Ministry for Education and Research (BMBF), the Max Planck Society, the French Ministry for Research, the CNRS-IN2P3 and the Astroparticle Interdisciplinary Programme of the CNRS, the UK Science and Technology Facilities Council (STFC), the IPNP of the Charles University, the Polish Ministry of Science and Higher Education, the South African Department of Science and Technology and National Research Foundation, and by the University of Namibia. We appreciate the excellent work of the technical support staff in Berlin, Durham, Hamburg, Heidelberg, Palaiseau, Paris, Saclay, and in Namibia in the construction and operation of the equipment.

Appendix A: Observations summary

The journal of observations for the 2005-2007 is presented in Table A.1.

Table A.1. Summary of the 2005 to 2007 observations.

MJD	θ_z	T	n_{on}	n_{off}	Excess	σ	$\sigma/\sqrt{T}$
53618	16.9	0.87	860	3202	219.6	7.5	8.0
53637	16.6	1.09	788	2673	253.4	9.2	8.8
53638	14.7	2.18	1694	6029	488.2	12.0	8.1
53665	22.6	0.87	618	2487	120.6	4.7	5.1
53666	26.3	1.31	857	3406	175.8	5.9	5.1
53668	23.3	1.30	926	3793	167.4	5.3	4.7
53669	19.6	0.86	1027	2939	439.2	14.7	15.8
53705	55.6	0.88	512	2542	3.6	0.1	0.2
53916	13.7	0.88	993	3317	329.6	10.7	11.5
53917	11.8	0.88	933	3163	300.4	10.1	10.7
53918	10.2	1.32	1491	4596	571.8	15.5	13.5
53919	10.9	1.32	1477	4638	549.4	14.9	13.0
53941	14.4	1.31	2445	4844	1476.2	35.0	30.6
53942	13.7	1.76	2453	5766	1299.8	29.5	22.3
53943	9.8	1.33	1142	3627	416.6	12.8	11.1
53944	13.2	1.33	12 762	3563	12 049.4	172.9	149.7
53945	23.9	5.23	8037	16 352	4766.6	62.0	27.1
53946	27.7	6.61	35 874	19 881	31,897.8	251.3	97.7
53947	25.1	5.89	17 158	17 006	13 756.8	142.6	58.8
53948	27.7	2.75	5366	7957	3774.6	64.6	38.9
53950	26.6	3.51	5108	11 955	2717.0	42.8	22.9
53951	28.4	2.51	3275	8421	1590.8	30.6	19.3
53952	35.8	1.76	1786	5395	707.0	17.7	13.3
53953	44.1	0.89	670	2285	213.0	8.4	8.9
53962	27.6	0.89	534	2088	116.4	4.9	5.3
53963	19.4	1.75	1613	6145	384.0	9.5	7.1
53964	10.3	1.49	1057	4146	227.8	6.9	5.6
53965	15.7	1.57	1584	5662	451.6	11.4	9.1
53966	18.6	0.88	719	2844	150.2	5.5	5.8
53967	24.3	0.86	481	1801	120.8	5.5	5.9
53968	19.1	0.86	479	1974	84.2	3.7	4.0
53969	21.2	1.29	1738	4368	864.4	23.0	20.2
53970	20.9	0.88	690	2759	138.2	5.1	5.5
53971	19.8	1.32	1449	4313	586.4	16.3	14.2
53972	16.5	1.30	683	2499	183.2	7.0	6.1
53973	14.5	1.32	1157	4311	294.8	8.6	7.5
53974	16.2	1.76	1504	5925	319.0	8.1	6.1
53975	15.8	0.88	804	3059	192.2	6.7	7.2
53976	13.8	0.89	727	2544	218.2	8.2	8.7
53977	12.0	0.88	832	2745	283.0	10.1	10.8
53978	13.3	0.89	687	2317	223.6	8.7	9.3
53995	21.4	1.75	1712	5989	514.2	12.6	9.5
53996	25.3	1.33	680	2834	113.2	4.2	3.6
53997	26.3	1.32	1113	4382	236.6	7.0	6.1
53998	26.1	1.32	1247	4082	430.6	12.6	11.0
53999	21.4	1.32	1107	4262	254.6	7.5	6.6

Table A.1. continued.

MJD	θ_z	T	n_{on}	n_{off}	Excess	σ	$\sigma/\sqrt{T}$
54264	8.5	0.13	109	449	19.2	1.8	5.0
54265	8.5	1.05	920	3513	217.4	7.1	6.9
54266	9.3	1.39	1129	4553	218.4	6.3	5.4
54267	9.2	1.32	1095	4176	259.8	7.8	6.7
54268	10.2	0.32	261	1040	53.0	3.2	5.6
54269	9.1	0.89	908	2491	409.8	14.7	15.6
54270	10.8	0.44	565	1266	311.8	14.9	22.4
54271	7.6	0.36	308	983	111.4	6.6	11.0
54294	7.7	0.44	447	1337	179.6	9.0	13.5
54296	7.2	0.44	350	1289	92.2	4.9	7.4
54297	9.8	0.44	344	1265	91.0	4.9	7.4
54299	7.6	0.44	347	1232	100.6	5.5	8.2
54300	7.3	0.44	343	1245	94.0	5.1	7.6
54302	7.7	0.44	358	1234	111.2	6.0	9.0
54304	7.9	0.88	680	2765	127.0	4.7	5.0
54319	8.9	0.88	692	2650	162.0	6.1	6.5
54320	8.0	0.89	553	2199	113.2	4.7	5.0
54329	11.7	0.44	297	1258	45.4	2.5	3.8
54332	7.0	0.16	100	391	21.8	2.1	5.3
54375	9.4	1.27	811	3124	186.2	6.4	5.7
54376	7.9	0.68	395	1605	74.0	3.6	4.4

Notes. For each night MJD is the Modified Julian Date, θ_z the mean observation zenith angle (degrees), T the total observation live-time (hours), n_{on} the number of on-source events, n_{off} the number of off-source events (from a region five times larger than for the on-source events). The final three columns are the corresponding excess, significance (given in units of standard deviations), and the significance per square root of the live-time.

Appendix B: Spectral variability

The numerical information associated with Fig. 7 is given in Tables B.1 (left panel, grey points), B.2 (left panel, black points) and B.3 (right panel). In addition, numerical information associated with Fig. 8 is given in Table B.4.

Table B.1. Integral flux (10^{-11} cm^{-2} s^{-1}) in the 0.2−1 TeV energy range versus photon index corresponding to grey points in the left panel of Fig. 7.

Φ	Index Γ
2.36 ± 0.13	3.345 ± 0.20
3.92 ± 0.17	3.64 ± 0.16
5.33 ± 0.22	3.46 ± 0.13
8.29 ± 0.30	3.64 ± 0.10
13.82 ± 0.82	3.82 ± 0.17

Notes. Errors are statistical. See Sect. 4.1 for more details.

Table B.2. Integral flux (10^{-11} cm^{-2} s^{-1}) in the 0.2−1 TeV energy range versus photon index corresponding to black points in the left panel of Fig. 7.

Φ	Index Γ
8.4 ± 0.3	3.74 ± 0.11
16.9 ± 0.5	3.82 ± 0.10
24.5 ± 0.7	3.78 ± 0.08
37.4 ± 1.0	3.77 ± 0.08
39.7 ± 1.1	3.76 ± 0.08
46.4 ± 1.1	3.66 ± 0.08
53.5 ± 1.3	3.57 ± 0.07
78.6 ± 1.9	3.44 ± 0.06
91.8 ± 1.9	3.33 ± 0.06
101.6 ± 2.8	3.30 ± 0.07
111.7 ± 3.0	3.33 ± 0.07
154.1 ± 3.5	3.28 ± 0.06
173.1 ± 3.8	3.16 ± 0.06
198.5 ± 3.8	3.28 ± 0.05
210.9 ± 3.9	3.14 ± 0.05

Notes. Errors are statistical. See Sect. 4.1 for more details.

Table B.3. Integral flux (10^{-11} cm^{-2} s^{-1}) in the 0.2−1 TeV energy range versus photon index corresponding to the right panel of Fig. 7.

Φ	Index Γ
4.2 ± 0.1	3.52 ± 0.07
17.3 ± 0.5	3.89 ± 0.09
38.6 ± 1.1	3.80 ± 0.08
43.6 ± 1.1	3.60 ± 0.07
51.5 ± 1.3	3.53 ± 0.07
67.2 ± 1.9	3.64 ± 0.07
86.1 ± 1.9	3.38 ± 0.06
97.0 ± 1.9	3.30 ± 0.05
111.7 ± 3.0	3.33 ± 0.07
154.1 ± 3.5	3.28 ± 0.06
173.1 ± 3.8	3.16 ± 0.06
198.5 ± 3.8	3.28 ± 0.05
210.9 ± 3.9	3.14 ± 0.04

Notes. Errors are statistical. See Sect. 4.1 for more details.

Table B.4. MJD, integral flux (10^{-11} cm^{-2} s^{-1}) in the 0.2−1 TeV energy range, and photon index corresponding to the entries of Fig. 8.

MJD	Φ	Index Γ
53944.02742 ± 0.00277	188.6 ± 30.6	3.22 ± 0.09
53944.03298 ± 0.00277	184.1 ± 30.9	3.28 ± 0.09
53944.03854 ± 0.00277	191.7 ± 32.6	3.45 ± 0.09
53944.04409 ± 0.00277	252.4 ± 40.5	3.19 ± 0.09
53944.04965 ± 0.00277	237.5 ± 33.8	3.16 ± 0.08
53944.05520 ± 0.00277	212.8 ± 30.8	3.04 ± 0.08
53944.06076 ± 0.00277	190.9 ± 30.0	3.09 ± 0.09
53944.06909 ± 0.00555	99.5 ± 17.5	3.18 ± 0.10
53944.98298 ± 0.05277	9.2 ± 3.1	3.89 ± 0.18
53945.04965 ± 0.01388	34.2 ± 8.3	3.83 ± 0.13
53945.07604 ± 0.01250	42.6 ± 10.2	3.92 ± 0.13
53945.93020 ± 0.00277	206.9 ± 34.9	3.2 ± 0.10
53945.93715 ± 0.00416	190.9 ± 28.6	3.15 ± 0.09
53945.94409 ± 0.00277	171.0 ± 30.5	3.23 ± 0.10
53945.94965 ± 0.00277	161.2 ± 28.2	3.06 ± 0.10
53945.95659 ± 0.00416	173.9 ± 28.9	3.35 ± 0.09
53945.96354 ± 0.00277	179.1 ± 29.4	3.11 ± 0.10
53945.97048 ± 0.00416	127.8 ± 22.6	3.36 ± 0.10
53945.98159 ± 0.00694	91.9 ± 16.5	3.42 ± 0.10
53945.99687 ± 0.00833	101.6 ± 16.9	3.12 ± 0.10
53946.00937 ± 0.00416	104.4 ± 19.7	3.28 ± 0.11
53946.01909 ± 0.00555	92.2 ± 17.1	3.37 ± 0.10
53946.03020 ± 0.00555	79.5 ± 15.9	3.42 ± 0.11
53946.03992 ± 0.00416	105.6 ± 19.3	3.26 ± 0.10
53946.04965 ± 0.00555	114.7 ± 20.9	3.45 ± 0.10
53946.05937 ± 0.00416	110.2 ± 19.6	3.17 ± 0.10
53946.06909 ± 0.00555	97.2 ± 19.9	3.54 ± 0.11
53946.08298 ± 0.00833	75.1 ± 12.8	3.24 ± 0.10
53946.09826 ± 0.00694	75.1 ± 15.5	3.55 ± 0.12
53946.93437 ± 0.00972	58.1 ± 13.5	3.92 ± 0.13
53946.95381 ± 0.00972	50.7 ± 11.2	3.6 ± 0.12
53946.97604 ± 0.01250	39.7 ± 8.7	3.62 ± 0.12
53947.00242 ± 0.01388	34.0 ± 7.5	3.62 ± 0.12
53947.02742 ± 0.01111	40.4 ± 8.8	3.56 ± 0.12
53947.04965 ± 0.01111	43.5 ± 10.3	3.82 ± 0.13
53947.07742 ± 0.01666	45.8 ± 10.1	3.75 ± 0.12

Notes. Only points associated with an energy threshold lower than 200 GeV are considered. Errors are statistical. See Sect. 4.2 for more details.

References

Aharonian, F., Akhperjanian, A., Beilicke, M., et al. (HEGRA. Collaboration) 2002, A&A, 393, 89

Aharonian, F., Akhperjanian, A. G., Aye, K.-M., et al. (HESS Collaboration) 2005a, A&A, 437, 95

Aharonian, F., Akhperjanian, A. G., Aye, K.-M., et al. (HESS Collaboration) 2005b, A&A, 430, 865

Aharonian, F., Akhperjanian, A. G., Bazer-Bachi, A. R., et al. (HESS Collaboration) 2005c, A&A, 442, 895

Aharonian, F., Akhperjanian, A. G., Bazer-Bachi, A. R., et al. (HESS Collaboration) 2006, A&A, 457, 899

Aharonian, F., Akhperjanian, A. G., Bazer-Bachi, A. R., et al. (HESS Collaboration) 2007a, ApJ, 664, L71

Aharonian, F., Akhperjanian, A. G., Barres de Almeida, U., et al. (HESS Collaboration) 2007b, A&A, 475, L9

Aharonian, F., Akhperjanian, A. G., Barres de Almeida, U., et al. (HESS Collaboration) 2008a, Phys. Rev. Lett., 101, 170402

Aharonian, F., Akhperjanian, A. G., Barres de Almeida, U., et al. (HESS Collaboration) 2008b, Phys. Rev. Lett, 101, 261104

Aharonian, F., Akhperjanian, A. G., Anton, G., et al. (HESS Collaboration) 2009, A&A, 502, 749

Aitchinson, J., & Brown, J. A. C. 1963, The Lognormal Distribution (Cambridge: Cambridge University Press)

Albert, J., Aliu, E., Anderhub, H., et al. (MAGIC Collaboration) 2007, ApJ, 669, 862

Arévalo, P., & Uttley, P. 2006, MNRAS, 367, 801

Begelman, M. C., Fabian, A. C., & Rees, M. J. 2008, MNRAS, 384, L19

Boutelier, T., Henri, G., & Petrucci, P. O. 2008, MNRAS, 390, 73

Chadwick, P. M., Lyons, K., McComb, T. J. L., et al. 1999, ApJ, 513, 161

Cheng, K. S., Zhang, X., & Zhang, L. 2000, ApJ, 537, 80

Djannati-Ataï, A., Piron, F., Barrau, A., et al. 1999, A&A, 350, 17

Edelson, R. A., & Krolik, J. H. 1988, ApJ, 333, 646

Edelson, R., Turner, T. J., Pounds, K., et al. 2002, ApJ, 568, 610

Fichtel, C. 1996, A&AS, 120, 23

Fossati, G., Celotti, A., Chiaberge, M., et al. 2000, ApJ, 541, 153

Ghisellini, G., & Tavecchio, F. 2008, MNRAS, 386, 28

Giebels, B., & Degrange, B. 2009, A&A, 503, 797

Giebels, B., Bloom, E. D., Focke, W., et al. 2002, ApJ, 571, 763

Giebels, B., et al. (HESS Collaboration) 2005, Proc. Annual meeting of the French Society of Astronomy and Astrophysics (Strasbourg), 527

Giebels, B., Dubus, G., & Khelifi, B. 2007, A&A, 462, 29

Gleissner, T., Wilms, J., Pottschmidt, K., et al. 2004, A&A, 414, 1091

Katarzyński, K., Lenain, J.-P., Zech, A., Boisson, C., & Sol, H. 2008, MNRAS, 390, 371

Kataoka, J. 1999, X-ray Study of Rapid Variability in TeV Blazars and the Implications on Particle Acceleration in Jets, ISAS RN 710

Kataoka, J., Takahashi, T., Wagner, S. J., et al. 2001, ApJ, 560, 659

Lemoine-Goumard, M., Degrange, B., & Tluczykont, M. 2006, Astropart. Phys., 25, 195

Levinson, A. 2007, ApJ, 671, L29

Lichti, G. G., Bottacini, E., Ajello, M., et al. 2008, A&A, 486, 721

Lyubarskii, Y. E. 1997, MNRAS, 292, 679

Maraschi, L., et al. 2002, Proc. Symposium "New Visions of the X-ray Universe in the XMM-Newton and Chandra Era", ESTEC 2001 [arXiv:0202418v1]

M^{c}Hardy, I. M., Papadakis, I. E., Uttley, P., Page, M. J., & Mason, K. O. 2004, MNRAS, 348, 783

Nandikotkur, G., Jahoda, K. M., Hartman, R. C., et al. 2007, ApJ, 657, 706

Nandra, K., George, I. M., Mushotzky, R. F., Turner, T. J., & Yaqoob, T. 1997, ApJ, 476, 70

Paltani, S., Courvoisier, T. J.-L., Blecha, A., & Bratschi, P. 1997, A&A, 327, 539

Piron, F., Djannati-Atai, A., Punch, M., et al. 2001, A&A, 374, 895

Poutanen, J., & Stern, B. E. 2008, Int. J. Mod. Phys., 17, 1619

Rutman, J. 1978, Proc. IEEE, 66, 1048

Simonetti, J. H., Cordes, J. M., & Heeschen, D. S. 1985, ApJ, 296, 46

Sreekumar, P., Bertsch, D. L., Dingus, B. L., et al. 1998, ApJ, 494, 523

Stecker, F. W., & Salamon, M. H. 1996, ApJ, 464, 600

Stern, B. E. 2003, MNRAS, 345, 590

Stern, B. E., & Poutanen, J. 2006, MNRAS, 372, 1217

Spada, M., Ghisellini, G., Lazzati, D., & Celotti, A. 2001, MNRAS, 325, 1559

Takahashi, T., Kataoka, J., Madejski, G., et al. 2000, ApJ, 542, L105

Uttley, P. 2004, MNRAS, 347, L61

Uttley, P., & M^{c} Hardy, I. M. 2001, MNRAS, 323, L26

Uttley, P., M^{c} Hardy, I. M., & Vaughan, S. 2005, MNRAS, 359, 345

van der Klis, M. 1997, Proc. Conf. Statistical Challenges in Modern Astronomy II, Pennsylvania State University (Berlin: Springer-Verlag), 321

Vaughan, S., Fabian, A. C., & Nandra, K. 2003a, MNRAS, 339, 1237

Vaughan, S., Edelson, R., Warwick, R. S., & Uttley, P. 2003b, MNRAS, 345, 1271

White, R. J., & Peterson, B. M. 1994, PASP, 106, 879

Zhang, Y. H., Celotti, A., Treves, A., et al. 1999, ApJ, 527, 719

[1] Max-Planck-Institut für Kernphysik, PO Box 103980, 69029 Heidelberg, Germany
e-mail: francesca.volpe@mpi-hd.mpg.de; volpe@llr.in2p3.fr
[2] Yerevan Physics Institute, 2 Alikhanian Brothers St., 375036 Yerevan, Armenia
[3] Centre d'Étude Spatiale des Rayonnements, CNRS/UPS, 9 Av. du Colonel Roche, BP 4346, 31029 Toulouse Cedex 4, France
[4] Universität Hamburg, Institut für Experimentalphysik, Luruper Chaussee 149, 22761 Hamburg, Germany
[5] Institut für Physik, Humboldt-Universität zu Berlin, Newtonstr. 15, 12489 Berlin, Germany
[6] LUTH, Observatoire de Paris, CNRS, Université Paris Diderot, 5 place Jules Janssen, 92190 Meudon, France
[7] CEA Saclay, DSM/IRFU, 91191 Gif-Sur-Yvette Cedex, France
[8] University of Durham, Department of Physics, South Road, Durham DH1 3LE, UK
[9] Unit for Space Physics, North-West University, Potchefstroom 2520, South Africa
[10] Laboratoire Leprince-Ringuet, École Polytechnique, CNRS/IN2P3, 91128 Palaiseau, France
[11] Laboratoire d'Annecy-le-Vieux de Physique des Particules, Université de Savoie, CNRS/IN2P3, 74941 Annecy-le-Vieux, France
[12] Astroparticule et Cosmologie (APC), CNRS, Université Paris 7 Denis Diderot, 10 rue Alice Domon et Léonie Duquet, 75205 Paris Cedex 13, France UMR 7164 (CNRS, Université Paris VII, CEA, Observatoire de Paris)
e-mail: santiago.pita@apc.univ-paris7.fr
[13] Dublin Institute for Advanced Studies, 5 Merrion Square, Dublin 2, Ireland
[14] Landessternwarte, Universität Heidelberg, Königstuhl, 69117 Heidelberg, Germany
[15] Laboratoire de Physique Théorique et Astroparticules, Université Montpellier 2, CNRS/IN2P3, CC 70, Place Eugène Bataillon, 34095 Montpellier Cedex 5, France
[16] Universität Erlangen-Nürnberg, Physikalisches Institut, Erwin-Rommel-Str. 1, 91058 Erlangen, Germany
[17] Laboratoire d'Astrophysique de Grenoble, INSU/CNRS, Université Joseph Fourier, BP 53, 38041 Grenoble Cedex 9, France
[18] Institut für Astronomie und Astrophysik, Universität Tübingen, Sand 1, 72076 Tübingen, Germany
[19] LPNHE, Université Pierre et Marie Curie Paris 6, Université Denis Diderot Paris 7, CNRS/IN2P3, 4 place Jussieu, 75252 Paris Cedex 5, France
[20] Charles University, Faculty of Mathematics and Physics, Institute of Particle and Nuclear Physics, V Holešovičkách 2, 180 00 Prague 8, Czech Republic
[21] Institut für Theoretische Physik, Lehrstuhl IV: Weltraum und Astrophysik, Ruhr-Universität Bochum, 44780 Bochum, Germany
[22] University of Namibia, Department of Physics, Private Bag 13301, Windhoek, Namibia
[23] Obserwatorium Astronomiczne, Uniwersytet Jagielloński, ul. Orla 171, 30-244 Kraków, Poland
[24] Nicolaus Copernicus Astronomical Center, ul. Bartycka 18, 00-716 Warsaw, Poland
[25] School of Physics & Astronomy, University of Leeds, Leeds LS2 9JT, UK
[26] School of Chemistry & Physics, University of Adelaide, Adelaide 5005, Australia
[27] Toruń Centre for Astronomy, Nicolaus Copernicus University, ul. Gagarina 11, 87-100 Toruń, Poland
[28] Instytut Fizyki Jądrowej PAN, ul. Radzikowskiego 152, 31-342 Kraków, Poland
[29] Astronomical Observatory, The University of Warsaw, Al. Ujazdowskie 4, 00-478 Warsaw, Poland
[30] Institut für Astro- und Teilchenphysik, Leopold-Franzens-Universität Innsbruck, 6020 Innsbruck, Austria
[31] Oskar Klein Centre, Department of Physics, Stockholm University, Albanova University Center, 10691 Stockholm, Sweden
[32] Oskar Klein Centre, Department of Physics, Royal Institute of Technology (KTH), Albanova, 10691 Stockholm, Sweden
[33] Department of Physics and Astronomy, The University of Leicester, University Road, Leicester, LE1 7RH, UK
[34] European Associated Laboratory for Gamma-Ray Astronomy, jointly supported by CNRS and MPG